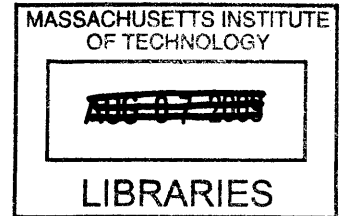# Methodology, Morphology, and Optimization of Carbon Nanotube Growth for Improved Energy Storage in a Double Layer Capacitor

by

Daniel C. Ku

B.S., Electrical Engineering
United States Naval Academy (2007)

Submitted to the Department of Electrical Engineering and Computer Science
in partial fulfillment of the requirements for the degree of
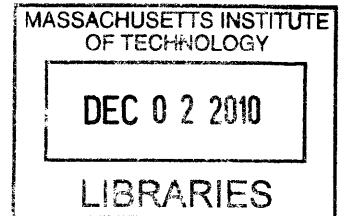
Master of Science

at the

ARCHIVES

Massachusetts Institute of Technology

June 2009

© 2009 Massachusetts Institute of Technology
All rights reserved.

Signature of Author............................
Department of Electrical Engineering and Computer Science
June 8, 2009

Certified by....................................
Joel E. Schindall
Bernard M. Gordon Professor of Electrical Engineering
Thesis Supervisor

Certified by....................................
John G. Kassakian
Professor of Electrical Engineering
Thesis Supervisor

Accepted by....................................
Professor Terry P. Orlando
Chair, Department Committee on Graduate Students
Department of Electrical Engineering and Computer Science

Methodology, Morphology, and Optimization of Carbon Nanotube Growth for Improved Energy Storage in a Double Layer Capacitor

by

Daniel C. Ku

Submitted to the Department of Electrical Engineering and Computer Science
in partial fulfillment of the requirements for the degree of
Master of Science

Abstract

The goal of this thesis is to optimize the growth of carbon nanotubes (CNTs) on a conducting substrate for use as an electrode to improve energy density in a double-layer capacitor. The focus has been on several areas, such as substrate material, growth conditions, catalyst variations, and thin-film deposition techniques in order to achieve growth of a high density, vertically-aligned carbon nanotube array suitable for use as an electrode. This thesis describes the methodology of modifying a significant number of parameters in order to achieve all of the targeted electrode specifications, with the exception of nanotube density. The successful growth of a CNT array on an aluminum foil substrate marks an important milestone for realizing a future commercial product.

Thesis Supervisor: Joel E. Schindall
Title: Bernard M. Gordon Professor of Electrical Engineering

Thesis Supervisor: John G. Kassakian
Title: Professor of Electrical Engineering

Acknowledgements

Table of Contents

List of Figures

List of Tables

1 Introduction

The focus of this thesis is on optimizing the growth of carbon nanotubes on a conducting substrate for use as an electrode to improve energy density in a double-layer capacitor. We have concentrated on several areas, such as substrate material, growth conditions, catalyst variations, and thin-film deposition techniques in order to achieve growth of a high density, vertically-aligned carbon nanotube array suitable for use as an electrode. This thesis describes the methodology of optimizing a significant number of parameters in order to achieve the targeted electrode specifications. By improving the electrode, we are able to improve the energy-density and power-density performance of double layer capacitors [1].

Although synthesis of an array of vertically aligned carbon nanotubes on silicon substrates has been well documented, there has been limited success in achieving the same growth results on metal substrates. This is primarily due to the catalyst-metal layer interactions that prevent the nanoparticles from nucleating [2]. The goals of this thesis are (1) to achieve direct CNT growth on a current collector suitable for use as an electrode, (2) to increase the density of the CNT array, (3) and to boost the carbon weight per cm^2, which reflects on the density, length, and number of walls for the CNTs. Targeted and achieved electrode specifications are given in Table 6.1.

1.1 Double Layer Capacitors

Double-layer capacitors (DLCs), also known as ultracapacitors, are a non-faradaic energy storage device, meaning that there is no exchange of charges between the electrode and electrolyte. The device obtains its name from the electrical double layer that is present at the interface between the electrodes and the electrolyte (see Figure 1.1). The specific capacitance of a DLC is many times larger than that of an ordinary dielectric capacitor for two reasons. First, a DLC has more than two orders of magnitude smaller

separation of charges between the electrode and electrolyte ions than possible with any dielectric material. Second, the electrodes of DLCs are made of a porous material, such as activated carbon, which has an effective surface area that is several orders of magnitude greater than the flat area of a parallel-plate capacitor (typically on the order of thousands of m^2 per gram). Unlike a traditional capacitor, ion mobility permits much of this surface area to be utilized.
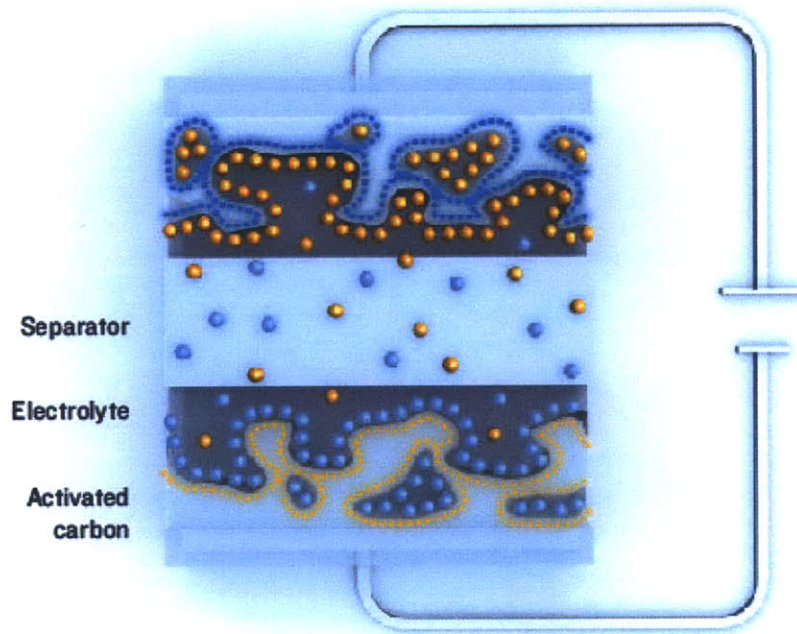
Figure 1.1: Cross-Section Representation of Double Layer Capacitor [3]

A DLC also has an extremely high breakdown field strength when compared to conventional capacitors. The close spacing and absence of avalanche dielectric breakdown allow DLCs to sustain significantly higher field strength across the double layer. This high field strength along with the increased specific capacitance allow DLCs to achieve high energy densities.

However, current DLCs based on activated carbon electrodes are limited in their energy density for several reasons. First, the irregular and uneven pore sizes of activated carbon particles decrease the effective surface area of the electrode by having some pores that are too small for electrolyte ions to penetrate and others that are too large to be utilized efficiently. Second, activated carbon contains impurities and dangling bonds due

to the activation process. While these impurities and dangling bonds may help increase the surface area, they also reduce the electrochemical stability of the carbon/electrolyte interface, resulting in a lower voltage rating. Third, activated carbon electrodes require a binder to connect the electrode to the current collector, introducing a contact resistance. Lastly, the binder is only capable of handling a limited voltage before interacting with the electrolyte, further limiting the energy storage of the device.

The cell's power density, though high compared to batteries, is limited by the reduced mobility of electrolyte ions through an uneven path in activated carbon. The poor conductivity of activated carbon further exacerbates the problem, adding to the contact resistance of the binder and creating a larger internal resistance.

The ideal DLC electrode should maximize energy density as well as power density. To maximize energy density, the electrode should have a high surface area that is readily accessible and an ability to sustain higher voltages without undergoing faradaic reactions or premature aging. To maximize power density, the electrode should have a structure with a well-defined path for ions to flow, as well as having low resistance.

1.2 Nanotube-enhanced Ultracapacitor Design and Structure

The nanotube-enhanced ultracapacitor (NEU) that we propose builds upon the structure of commercial ultracapacitors, but replaces the activated carbon coated electrode with an electrode structure based on vertically aligned carbon nanotubes (VCNTs), shown in Figure 1.2 [4]. We postulate that vertically aligned carbon nanotubes that are directly grown on a conducting substrate (for use as an electrode) are able to achieve high energy and power density, and have the potential to fulfill all the requirements of an ideal DLC electrode. Carbon nanotubes (CNTs) exhibit a high surface area, are chemically stable, have excellent conductivity, and are lightweight. The open structure of an array of vertically aligned CNTs allows for the unobstructed flow of ions in and out of the active layer. Direct growth of the CNT electrode on the current collector

15

eliminates the need for a binder, as well as improving conductivity and decreasing internal resistance.
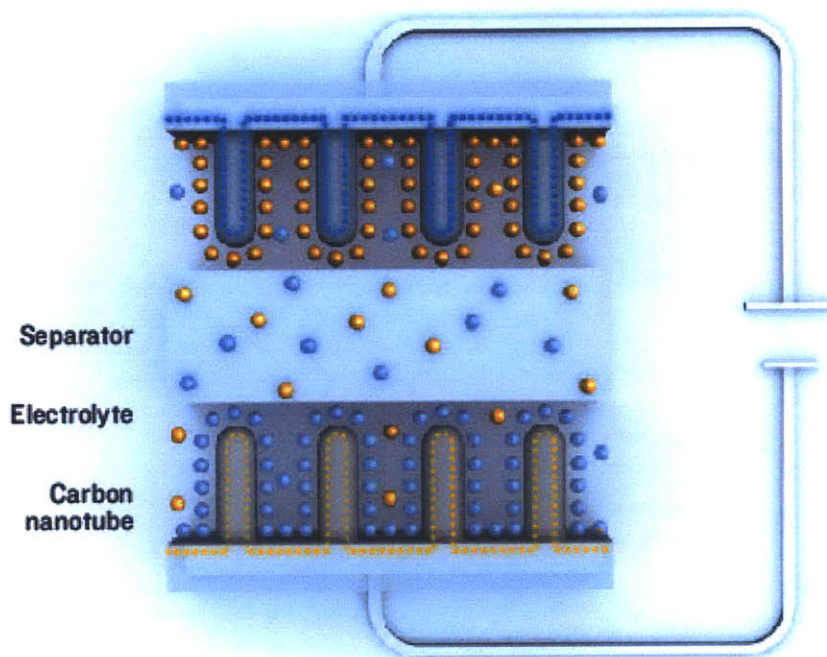
Figure 1.2: NEU structure with electrodes using VCNTs [3]

The vertical structure of the CNT array provides a clear path for ions to travel, which has been demonstrated to increase the power density. The relatively uniform spacing of the CNT walls avoids the unused micropores present in activated carbon devices, which is predicted to increase the energy density. The binder-free electrode allows for higher chemical stability and operation at a higher voltage rating. In addition, the direct growth of the CNTs on the current collector results in a reduction of the contact resistance between the current collector and the active layer. The direct growth process is also better suited for future manufacturing. By eliminating the need to grow CNTs on a silicon substrate and subsequently transfer them to an electrode, a potentially difficult and expensive step is avoided.

Commercial ultracapacitors using activated carbon have already been demonstrated to achieve power densities far greater than lithium ion (Li-ion) batteries because batteries are rate-limited by faradaic reactions. The primary limitation of commercial

ultracapacitors has been their relatively low energy densities compared to Li-ion batteries (typically on the order of 5%). Nanotube-enhanced ultracapacitors (NEU) could potentially approach the energy density of Li-ion batteries because of their increased specific capacitance and operating voltage. Moreover, the NEU is projected to achieve even greater power density than current commercial ultracapacitors because of its direct ion path and lack of a binder. In addition, ultracapacitors also do not undergo faradaic charge exchanges. As such, the NEU is predicted to be able to withstand hundreds of thousands of charge/discharge cycles, as is already the case in commercial ultracapacitors. This represents a critical improvement over current batteries. The absence of faradaic reactions also minimizes the temperature dependence of ultracapacitors. The potential improvements of the NEU over commercial DLCs and Li-ion batteries are summarized in Table 1.1 below.

Table 1.1: Comparison of Competing Energy Storage Devices

	Commercial DLC (typical)	Li-ion battery (typical)	MIT NEU (projected)
Energy Density (Wh/kg)	5.5	140	20-40
Power Density (kW/kg)	5.5	1	30
Rated Voltage (V)	2.7	3.6	3.5
Charge Cycles	>500,000	300-3000	>500,000
Robustness and Reliability	Excellent	Moderate	Excellent
Temperature Dependence	Minimal	Moderate to High	Minimal

1.3 Existing Research

There has been considerable effort in studying the growth of CNTs for a variety of applications, including use as electrodes in ultracapacitors. Through these efforts, growth

of vertically aligned CNTs on silicon (Si) substrates with a transition metal of either nickel (Ni), cobalt (Co), or iron (Fe) as the catalyst has been well documented [5]. Aluminum oxide or alumina (Al_2O_3) is commonly used as the supporting substrate, which serves to prevent the catalyst and substrate from interacting and allows for catalytic nanoparticles to form. However, such a combination of materials is not suitable for use as electrodes due to poor conductivity of the substrate. It is important to note that almost all of the previous research on using CNTs as part of a DLC electrode has focused on indirect CNT growth methods that rely upon the transfer of CNTs grown on silicon to a current conducting substrate.

Niu et. al. first introduced the idea of a DLC using entangled multi-walled nanotubes (MWNTs), achieving an energy density of 0.56 Wh/kg based on the weight of the electrolyte, separator, and the two electrodes [6]. The Niu device utilized catalytically grown carbon nanotubes with an average diameter of 8.0 nm that were commercially produced by Hyperion Catalysis International. The CNTs were first pretreated with nitric acid, filtered, and then dried to form an electrode of randomly entangled and cross-linked nanotubes. After treatment, the BET-measured surface area increased from 250 m^2/g to 430 m^2/g. The BET method of measuring surface area is named after a method introduced by Brunauer, Emmett, and Teller [7]. It measures the adsorption and desorption of an inert gas by a material at various pressures in order to derive the surface area of the material. Using 38 wt. % H_2SO_4 as the electrolyte, the measured specific capacitance of the Niu device ranged from 113, 102, and 49 F/g at 0.001 Hz, 1 Hz, and 100 Hz, respectively. The 'knee' frequency, or maximum frequency at which capacitive behavior is dominant, was shown to be 100Hz, significantly higher than the 1 Hz knee frequency of most commercial DLCs.

An et. al. obtained higher energy and power densities by pasting single-walled nanotubes (SWNTs) to a thin Ni foil current collector [8]. The nanotube electrode consisted of 70 wt. % of randomly entangled and cross-linked SWNTs and 30 wt. % poly(vinylidene chloride) (PVDC) as the binder. The electrodes were then heat treated at temperatures up to 1000°C for 30 min. It was found that with increasing temperature, there is an increase in specific surface area and a decrease in average pore diameter. The maximum specific capacitance was measured as 180 F/g, with a power density of 20

kW/kg and an energy density of 6.5 Wh/kg. Although the measured BET surface area of 357 m^2/g was less than the 430 m^2/g reported in Niu's MWNT device, the improved performance was attributed to better surface area utilization through better pore size control.

The fabrication techniques discussed above were limited in their energy and power densities by either the need for pretreatment (Niu) or a binder (An), which increased parasitic resistances. Yoon et. al. was able to decrease contact resistance by directly growing CNTs on a Ni foil collector [9]. No catalyst was deposited on the foil and MWNTs were grown using the PECVD method with methane and hydrogen as the reactant gases. The nanotubes were then treated with a NH_3 plasma to remove impurities. After NH_3 treatment, the specific capacitance of the device increased from 38.7 F/g to 207 F/g with a corresponding surface area increase from 9.63 m^2/g to 86.5 m^2/g. The directly grown CNT electrodes also exhibited rectangular cyclic voltammograms at scan rates up to 1000 mV/s. However, the grown CNT array achieved a thickness of only 20nm, which is insufficient for viable energy storage purposes.

Researchers found it difficult to grow a sufficient CNT array on a conducting substrate, which led to in a number of different techniques for implanting previously grown CNTs onto a metal current collector. Du and Pan fabricated CNT electrodes by electrophoretic deposition (EPD) [10]. CNTs grown from another source are suspended in solution and deposited on a current collector under the influence of an electric field. The electrical resistance of the as-deposited EPD films is extremely high (~$k\Omega$); however, after annealing in a hydrogen environment, there is a drastic decrease in the resistance. This may be attributed to electrochemical oxidation that takes place during EPD, which is then reduced through hydrogen treatment. Du and Pan report near-ideal rectangular cyclic voltammograms at scan rates up to 1000 mV/s, a knee frequency of 7560 Hz, and a power density of 20 kW/kg. Specific capacitance is calculated to be 84 F/g.

Kumar et. al. have proposed a method of contact transfer of CNTs using low temperature solder alloys [11]. The process involves annealing a solder coated conducting substrate and placing it in close contact with a CNT array grown on a Si substrate. The CNTs then penetrate the solder surface and are entrapped and transferred after solidification of the solder. The use of solder provides a low contact resistance

between the CNTs and the current collector. This technique is capable of directly transferring an array of vertically aligned CNTs. However, a DLC produced using this method has not yet been reported. While transfer methods circumvent the need to directly grow CNTs on a metal current collector, producing DLCs using these techniques requires significant extra manufacturing steps as well as the need for a supply of CNTs from another source.

Recent advances have allowed for Hata et. al. to achieve millimeter-length growth of SWNTs on silicon substrates using a water-assisted "supergrowth" method [12]. This procedure uses water vapor as an agent to promote and preserve catalytic activity, thereby allowing for longer growth. The best reported result is a height of 2.5mm in 10 minutes of growth time. At several technical conferences, the same group has also introduced the idea of pressing down the CNT array in order to achieve a higher density. No further results have been reported.

Most recently, Futaba et. al. have produced a "SWNT solid": a highly dense, vertically aligned CNT structure [13]. It uses the surface tension of liquids to zip together a CNT forest grown on silicon. The zipping together of the CNTs demonstrates the need for greater density in the growth of CNTs to produce a greater surface area. The "SWNT solid" has a density on the order of 10^{12}, an average CNT diameter of 2.8 nm, and a BET surface area of 1000 m^2/g. An electrochemical cell was produced by sandwiching the SWNT solid between platinum sheets, using 1M tetraethylammonium tetrafluoroborate (Et_4NBF_4)/propylene carbonate electrolyte. From the reported data, the specific capacitance is estimated to be 60 F/g at 2.5V. The energy density is estimated to be 13 Wh/kg. The data suggests that much of BET surface area is unused and does not participate in charge storage. The mechanism behind the unused BET surface area has not been described.

Analysis of our proposed nanotube-enhanced ultracapacitor electrode structure suggests that a BET surface area of 500 m^2/g is achievable, which would allow for a specific capacitance several times higher than that of activated carbon based DLCs. Such an array would be comprised of CNTs with three walls and an average diameter of 6.5nm. Average spacing between the nanotube centers is 10 nm, which allows for a nanotube density of 10^{12} CNTs/cm^2. With an operating voltage of 3.5V (based on voltages

achieved with graphene), the device would obtain an energy density of up to 35 Wh/kg.

Table 1.2 below summarizes the reported experimental CNT electrode parameters.

Table 1.2: Summary of reported experimental CNT electrode parameters

Group	Voltage (V)	E_v (Wh/l)	E_g (Wh/kg)	C_g (F/g)	S_{bet_u} untreated (m^2/g)	S_{bet_t} treated (m^2/g)
Niu	1.0	3.1	3.9	113	250	430
An	0.9	3.8	6.5	180		357
Yoon	0.9		5.8	207		86.52
Du	1.0		2.9	84		
Futaba	2.5	10.4	13.0	60	1000	
MIT NEU (projected)	3.5	31	35	100-200	500	1350

E_v: Volumetric energy density of two electrode cell

E_g: Gravimetric energy density of two electrode cell

C_g: Gravimetric specific capacitance

S_{bet}: BET measured surface area

1.4 Organization of Thesis

Although CNTs can be used for a variety of applications, this thesis is focused on the growth of a dense CNT array for the specific purpose of using it as an electrode for an ultracapacitor. Chapter 2 lays out the framework for the process of synthesizing carbon nanotubes. Various methods of synthesizing CNTs are presented, along with the reasoning behind choosing the chemical vapor deposition (CVD) growth method. A model of the CVD growth method of CNTs is introduced, as well as an explanation of the growth process that we have developed. A method of calculating CNT density based

upon weight and surface area of the CNT array is also established. Chapter 3 deals with the choice of material for the current collector on which to synthesize CNTs. Beginning with silicon substrates, a baseline standard is determined. From there, experimental growth is performed on various types of conducting substrates, starting with thick tungsten substrates, moving to tungsten foil, and finally progressing to aluminum foil. Chapter 4 begins a discussion on the various ways to optimize the density of the CNT array. Several parameters are examined, including the material(s) used as a catalyst, the thickness of the catalyst layer, the role of the underlayer, the amount of hydrogen, and the temperature profile during growth. In chapter 5, the affect of different thin-film deposition techniques upon growth is investigated. In a research setting, there has been a heavy dependence on the method of electron beam (e-beam) evaporation in order to deposit our catalyst layer and underlayer. However, such a technique is not suitable on a larger scale. The differences between samples deposited using e-beam and those that are deposited using sputter deposition are examined. Finally, the last chapter provides a brief summary of results and accomplishments, as well as presenting some possible future directions of research.

2 Synthesis of Carbon Nanotubes

Various growth methods for carbon nanotubes are reviewed. A model for the mechanisms behind the nucleation and growth of carbon nanotubes is introduced. Our system for growing nanotubes is discussed, as well as our process for growth. Various methods to characterize CNT growth are examined, with a focus on a method of calculating the density of a CNT array.

2.1 Growth Methods of Carbon Nanotubes

There are several different methods to produce carbon nanotubes, including arc discharge, laser ablation, plasma-enhanced chemical vapor deposition (PECVD), and thermal chemical vapor deposition (CVD) [14].

The arc discharge and laser ablation methods are commonly used to provide small quantities of high quality carbon nanotubes. These two techniques represent the earliest method of growing CNTs and are expensive. Both methods require the evaporation of a carbon source. In the arc discharge method, two carbon electrodes are placed a small distance apart. A large current across a potential difference allows for the vaporization of the carbon on one electrode and the deposition of carbon nanotubes along with other carbon products on the surface of the other. Laser ablation uses a dual-pulsed laser to directly vaporize a carbon source, which is often mixed with a catalytic mixture of transition metals. Although both methods are relatively simple, they have low yields and need further purification to separate the nanotubes from other carbonaceous products [15].It is also unclear how to scale up the yield of nanotubes for industrial production. The nanotubes produced using these methods are often entangled, creating an undesirable structure for nanotube electrodes.

More recently, chemical vapor deposition (CVD) has been used to produce a large yield of nanotubes by decomposition of a hydrocarbon gas over a catalyst particle,

usually at a high temperature (700-1000°C) [16]. The PECVD method utilizes plasma enhancement in order to allow for lower temperature processing, since some substrates cannot handle the high temperatures of the CVD process. The CVD techniques represent a great improvement in yield and quality for the growth of CNTs, as well as a reduction in cost compared to arc discharge and laser ablation.

The CVD process allows for relatively independent control of a variety of parameters. Numerous studies have utilized the CVD process to examine the growth of CNTs by varying the catalyst, supporting underlayer, growth gases, growth temperature, annealing steps, etc [17]. Due to the extremely large variable space, the growth mechanisms for different processes are likely different [18]. Because of its high yield, scalability, and versatility, the CVD process is used as our growth procedure.

2.2 Growth Model

For the CVD process, the parameters affecting growth include catalyst concentration, temperature, growth time, gas composition, flow rate, and growth pressure. The effect of parameter variation and interaction on the carbon nanotube growth mechanism and kinetics are not fully understood. As a result, there are numerous models of catalytic growth of CNTs [17][19][20][21].

CNT formation can be broken into three distinct parts: nanoparticle formation, nucleation, and growth kinetics. The catalyst nanoparticle distribution determines the ultimate density of the CNTs. Nanoparticle formation depends heavily on how the catalyst layer was formed. The catalyst material, deposition technique, and catalyst thickness, as well as the smoothness of the substrate, all effect the formation of possible nanotube nucleation sites. The nucleation process controls whether a nanoparticle can support the formation of a CNT. It will determines the actual density of the CNT array. The growth kinetics process explains the continued adsorption and diffusion of carbon on

a nanoparticle that fuels and ultimately stops the growth of CNTs. It determines the overall CNT length.

The nucleation process is modeled by the diamond nucleation model [21][22]. The overall mechanism considers impingement of carbon atoms on the catalyst for the carbon-containing species, adsorption at the catalyst-hydrocarbon interface, diffusion on the surface and through the bulk of the catalyst, and the formation of a stable carbide. As a hydrocarbon species is introduced into an environment containing a catalyst, carbon atoms from the ambient begin to impinge upon the surface of the catalysts. The adsorption rate of the deposited carbon is determined by the impingement rate and the sticking coefficient of the hydrocarbon. As carbon atoms begin to build up on the surface of the catalyst, they also begin to diffuse through the catalyst and form carbide structures. If the carbide structure reaches a critical size, it will become stable and nucleation will have occurred. Otherwise, desorption and diffusion of the carbon will prevent a stable structure from forming.

Growth kinetics are dependent upon additional carbon flux from the hydrocarbon gas. As carbon is adsorbed and diffused through the catalyst, the CNT length grows. However, over time, catalytic activity is halted due to poisoning by hydrocarbon gas-phase pyrolysis products. The poisoning either over-coats or deactivates sites on the catalyst surface [17].

The temperature range of the thermal CVD process is more likely to yield multi-walled carbon nanotubes (MWNT) than single-walled carbon nanotubes (SWNT). [23]. SWNTs are more likely to be formed by other methods such as arc discharge, where the reactions take place at higher temperatures. The number of nanotube walls is related to both growth temperature and pressure, where higher temperature and lower pressures yield SWNT [17][23]. The size of the catalyst nanoparticle may also play a role in determining the number of CNT walls.

For our NEU electrode, MWNTs are preferred for several reasons. MWNTs are more likely to be conductive than SWNTs. Whether a nanotube is metallic or semi-conducting is determined by the direction in which the graphite sheet is rolled to form a nanotube cylinder, otherwise known as its chirality [24]. Because a MWNT contains multiple cylinders, it is more likely to contain a metallic layer. MWNT growth is more

robust because it can survive a defect in one of its layers. MWNTs will also allow for subsequent surface modifications without affecting conductivity.

Overall CNT diameter will roughly be equal to the diameter of the catalyst nanoparticle [20][21]. For a highly dense forest of CNTs, it is desirable to have the smallest diameter of catalyst nanoparticles that are still able to nucleate MWNTs. This would typically be on the order of 10 to 15 nm.

2.3 Synthesis Process

2.3.1 Low Pressure Chemical Vapor Deposition System

A low-pressure chemical vapor deposition facility (LP-CVD) was designed and built in the Laboratory for Electromagnetic and Electronic Systems (LEES) by Ph.D candidate Riccardo Signorelli [1]. The LP-CVD system allows for the growth of vertically aligned carbon nanotubes arrays directly onto a metal current collector. The system is entirely composed of stainless steel parts, including gas lines and other components. As such, a variety of hydrocarbon and carrier gases can be used for growth. Our setup currently uses argon (Ar), hydrogen (H_2) and acetylene (C_2H_2).

The system is composed of a vacuum pump, power supply, quartz growth chamber, high temperature resistive heating element, gas cabinet, LabVIEW computer control system, and safety sensors and equipment (see Figure 2.1). The vacuum pump is capable of lowering the background pressure in the growth chamber to below 10 mTorr, assuring a low level of impurities and allowing for better repeatability and reliability. The vacuum line consists of both low and high pressure control valves, allowing for greater pressure control inside the growth chamber. Because of the small size of the deposition chamber, the chamber can be quickly evacuated from atmospheric pressure to <20 mTorr in less than 30 seconds.

Inside the quartz growth chamber is a substrate resistive heating element, typically an extrinsic, p-type silicon substrate (see Figure 2.2) [25]. The heating element directly heats

26

the sample, and the temperature is controlled by the current flowing through the heating element (see Figure 2.2). Temperature of the heater is measured by an infrared sensor. Substrate samples were 1cm x 1cm squares; therefore, the heating element is also small, measuring 5 cm x 1.5 cm. The heater is therefore very sensitive to current, allowing for rapid changes of temperature. A flow chart of the CVD process and control valves is shown in Figure 2.3.
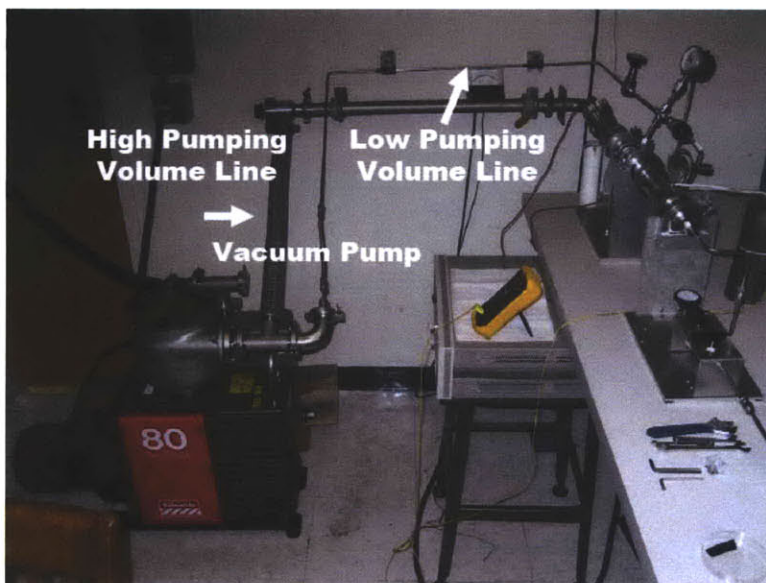
Figure 2.1: LP-CVD System
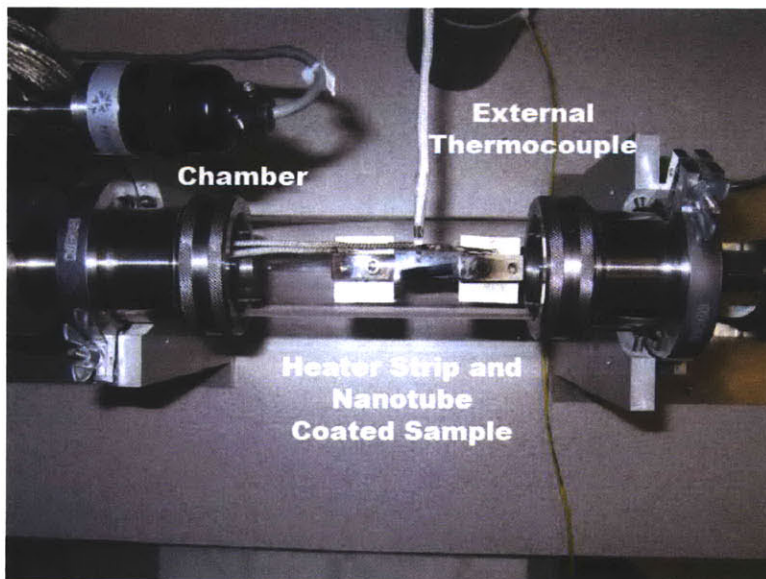
Figure 2.2: CVD Growth Chamber
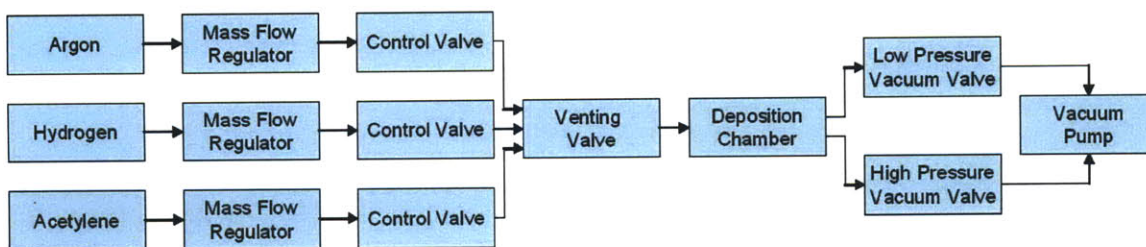
Figure 2.3: Flow chart of LP-CVD process setup

A screenshot of the LabVIEW controller program is shown in Figure 2.4. The LabVIEW software program was written by Fergus Hurley, a former graduate student. The LabVIEW controller program can be used either in a manual mode or computer-controlled mode. In the manual mode, the user inputs the amount of current sent to the heater, thereby controlling the temperature of the heater. This control is highlighted by the green box in Figure 2.4. The user also enters in the desired gas rate in the area highlighted by the red box. The blue boxed area displays the actual gas flow rate, as measured by the mass flow controllers.

In the computer-controlled mode, the LabVIEW program tracks the values entered into separate tables for both a gas profile and temperature profile. The gas profile and temperature profile are run independent of each other, and starting either profile will override the manual controls. The gas profile control is highlighted in a yellow box, while the temperature profile control is highlighted by the orange box.

The gas profile allows for the user to vary the amount of gas flow at any time. The gas flow rate is again shown in area highlighted by the blue box. For the temperature profile, the LabVIEW control program contains a proportional-integral-derivative (PID) controller system for maintaining a constant temperature, with the infrared sensor aimed at the heating element for the feedback loop. The temperature profile works on a linear

28

scale. For example, if the table has entries for t(1 min)=200°C and t(3 min)=400°C, the controller will increase temperature at a rate of 100°C/min until reaching 400°C at the 3rd minute.
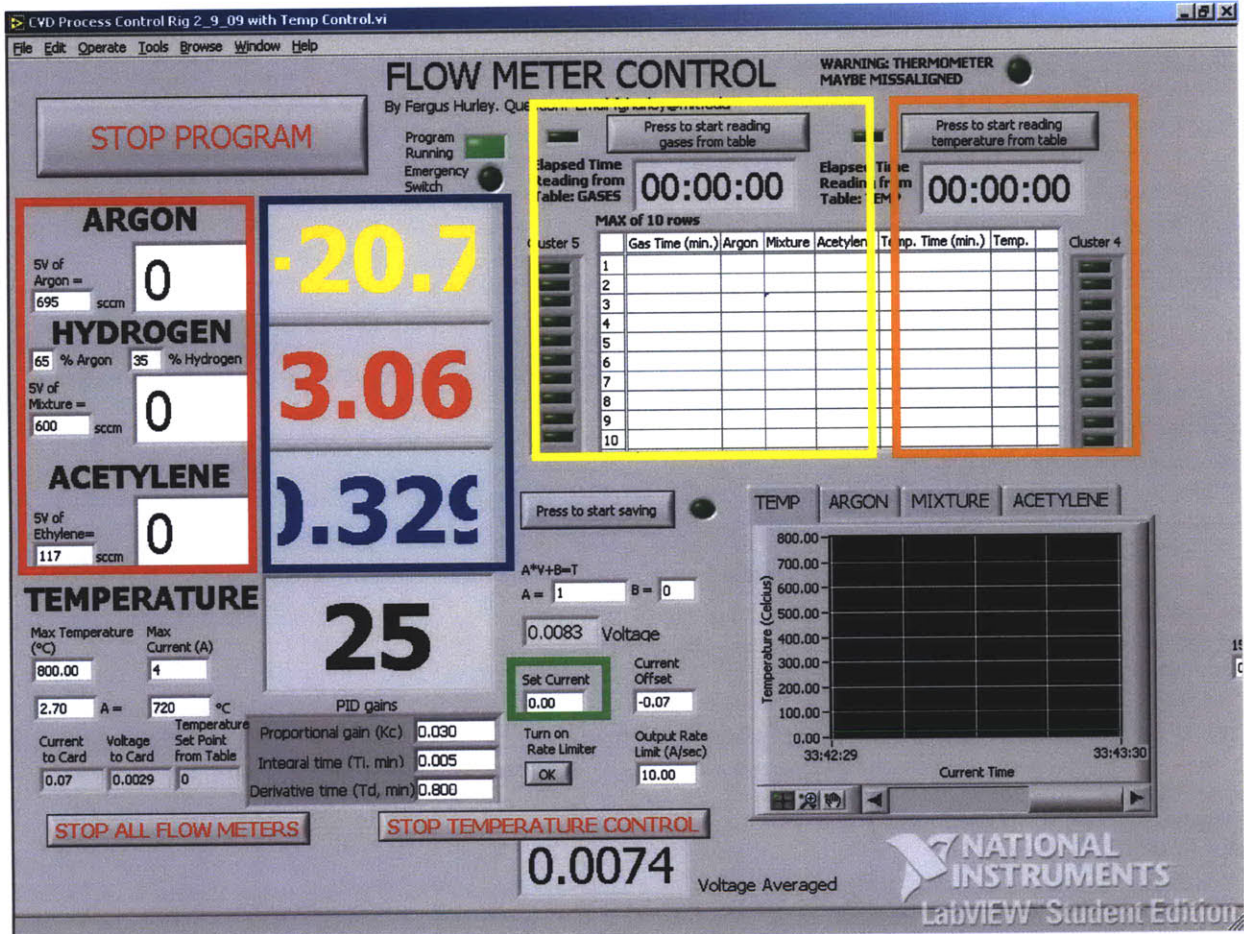
Figure 2.4: Screenshot of LabVIEW program with various controls highlighted by colored boxes. The green box is the manual control for current to the heater. The red box is the manual control for gas flow rate. The yellow and orange boxes are tables for computer-control of gas profile and temperature profile, respectively. The blue box displays the gas flow rate, as measured by the mass flow controllers.

2.3.2 Growth Procedure

The goal of growing a dense, nanotube forest is accomplished through several steps. First, the thin film of catalyst must coalesce into numerous small nanoparticles as the seeds for growth. Second, the nanoparticles must be "activated" so that a large percentage of them yield growth. Last, the growth must continue until the desired length is reached.

The thermal CVD process that we use to grow CNTs has been a constantly evolving process to find the optimal growing conditions for our specific application. Initial CNT growth experiments were performed on silicon (Si) substrates before moving on to various conducting substrates. Although silicon is not a conductive substrate, it was utilized as a baseline comparison test since robust growth of millimeter length, vertically aligned CNT arrays have been achieved on silicon substrates [26][27]. The progression from Si substrates to conducting substrates will be further expounded upon in a later chapter.

Based upon empirical data, changes in temperature, time, pressure, and rate of gas flow were evaluated and modified as necessary. At present, we have settled on a three part process for CNT fabrication, which is referred to as the OAG process: (1) oxidation, (2) annealing, (3) growth.

2.3.2.1 Oxidation

The first step in the OAG process is the oxidation of the deposited catalyst. This necessary step was added after it was observed that CNT yield was higher when the sample was allowed to rest for some time on a hot heater instead of a cool one (such as the time between sample runs). The oxidation step allows for the catalyst to oxidize due to the oxygen in the air. There is still debate as to whether an oxidized or metallic form of the catalyst is better for growth [28]. Our results indicate that first oxidizing the catalyst increases the growth rate.

For all experiments, the heater was first pre-heated to 325°C for 5 minutes. Due to thermal conductivity variations, a large current is necessary to initially heat the heater

from room temperature. This step ensured that the heater was pre-heated and that the same amount of current produced the same temperature during later steps.

For the oxidation step, the sample is placed on the heater in the deposition chamber. The sample is heated in an ambient air environment to the set oxidation temperature (varies, typically 200-400° C) for five minutes.

2.3.2.2 Anneal

The annealing step allows for stabilization. After oxidation, the deposition chamber is evacuated to a pressure <10 mTorr, and the sample is held at the annealing temperature (varies from 25-200° C, but < than oxidation temperature) for five minutes. The annealing step allows for the removal of adsorbed oxygen and nitrogen from the oxidation step and allows the newly formed catalyst nanoparticles to stabilize.

2.3.2.3 Growth

After annealing, the gases are allowed to flow for one minute to create a stable environment. In our experiments, the carrier gases were argon (Ar) and hydrogen (H_2) and the carbon-source gas was acetylene (C_2H_2). The pressure is then allowed to rise to 30 Torr by closing off the high vacuum line and the temperature is increased to the growth temperature (varies, typically 675°C). This environment is maintained for the set growth time. Visible nucleation of nanotubes, identified by the catalyst layer suddenly turning black, takes place in the low 600°'s temperature range.

The majority of experiments had a growth time of 30 minutes, although good growth can be achieved in as little as 15 minutes. For longer growth times, the growth rate gradually decreased over time due to catalyst poisoning. We found that 30 minutes was suitable to achieve our desired growth lengths (~150 μm), which is also approximately 2/3 of the maximum growth length (~250 μm). To end the experiment, all

gas flow except for argon is halted and the temperature is lowered to room temperature. As an inert gas, argon is used to refill the deposition chamber so that it can be opened to remove the sample.

A sample timeline of temperature profile, gas profile, and deposition chamber (not including heater pre-heat) is shown in Table 2.1. The source gases were used in a proportion of 3.7% C_2H_2 in 11% H_2 and 85.3% Ar. These percentages are similar to previously reported research [18]. Initial tests were performed at a gas flow rate of 350 sccm of Ar, 45 sccm of H_2, and 15 sccm of C_2H_2. These values did not produce sufficient growth, probably due to the low growth pressure. Therefore, gas flow rates were doubled to 700, 90, and 30 sccm for Ar, H_2 and C_2H_2, respectively. At these rates, the deposition chamber pressure is 50 mTorr, which is suitable for nanotube growth. Higher flow rates were not evaluated.

Table 2.1: Sample timeline for CVD growth procedure

Step	Time (min)	Temperature (°C)	Gas Flow Rate (sccm)			Chamber Pressure
			Ar	H_2	C_2H_2	
Heating to Oxidation Temp.	0-2	325	0	0	0	760 Torr
Oxidation	2-7	325	0	0	0	760 Torr
Annealing	7-12	400	0	0	0	<10 mTorr
Flow gases	12-13	400	700	90	30	1 Torr
Temp. ramp up for Growth, close high vacuum line	13-15	675	700	90	30	50 Torr
Growth	15-35	675	700	90	30	50 Torr
Cool Down	35-37	Decreasing	700	0	0	Increasing

2.4 CNT Characterization

CNTs were characterized using a variety of different methods. Important parameters include weight and thickness of the CNT array, as well as the number of walls and average diameter of each individual nanotube.

The weight of the CNT array was measured using a Sargent-Welch analytical balance by taking the change in weight of the substrate before and after growth. Electron microscopy techniques were used to image the CNTs. Scanning electron microscopy (SEM) was used image the CNT array thickness. High resolution transmission electron microscopy (TEM) was used to measure the CNT diameter and numbers of walls. Figure 2.5 shows a TEM image of a CNT with six walls and an average diameter of 7.6 nm.

The density of the CNT layer (CNTs/cm^2) can be estimated from analytical calculations or visual evidence from SEM imaging. Analytical calculations determine the CNT density (ρ_c) using the measured weight (W_c) of the CNT array and the average CNT diameter (d_c), height (h_c), and number of walls (N_c).

For a single-walled nanotube (SWNT), the surface area per gram is 1342 m^2/g. The weight of a single-walled nanotube (W_{SWNT}) can be determined by the surface area of the nanotube (S_{SWNT}) divided by the surface area per gram:

$$W_{SWNT} = \frac{S_{SWNT}}{1342} = \frac{d_c \bullet h_c \bullet \pi}{1342}$$

(2-1)

The density of nanotubes (ρ_c) can then be calculated by dividing the measured weight of the array (W_c) by the total weight of a nanotube ($W_{SWNT} \cdot N_c$ because of multiple walls).

$$\rho_c = \frac{W_c}{W_{SWNT} \cdot N_c} = \frac{W_c \cdot 1324}{N_c \cdot d_c \cdot h_c \cdot \pi}$$

(2-2)
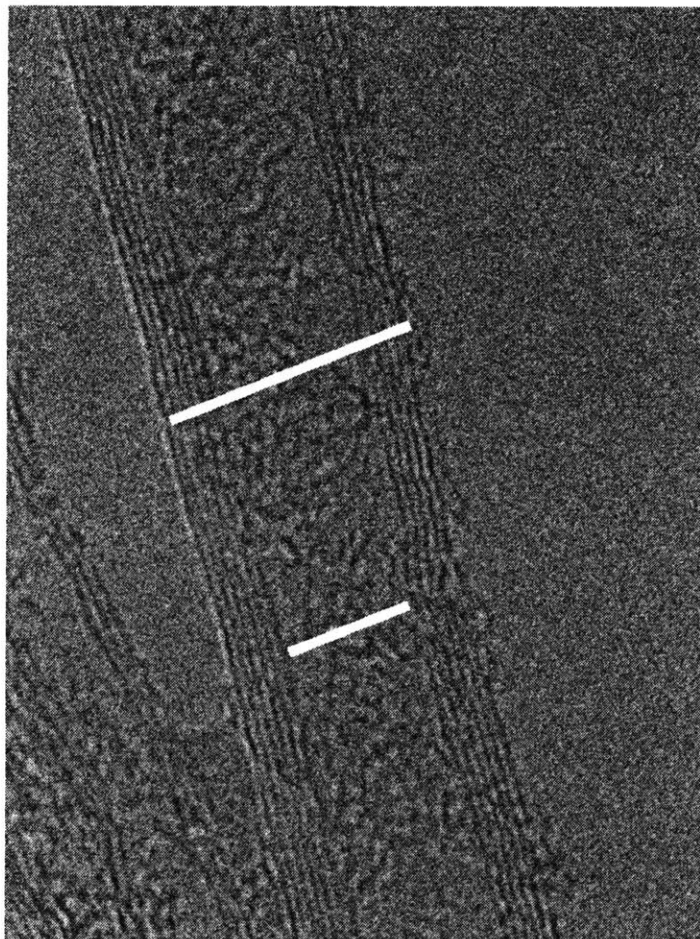
Figure 2.5: TEM Image of CNT with 6 walls. The outer diameter is 9.1 nm and the inner diameter is 5.5 nm. The image was taken using a JEOL TEM 2010 with CNTs dispersed on a copper grid. (Sample 042208-4, Image by R. Signorelli)

The analytical estimation of CNT density can be corroborated by visual evidence from high resolution SEM (HR-SEM) imaging. We have observed that when the CNT layer is removed by sonication, they leave behind holes where the individual nanotubes were originally located. By counting the number of holes per unit area, we can estimate the density of the CNT array, as shown in Figure 2.6 below.
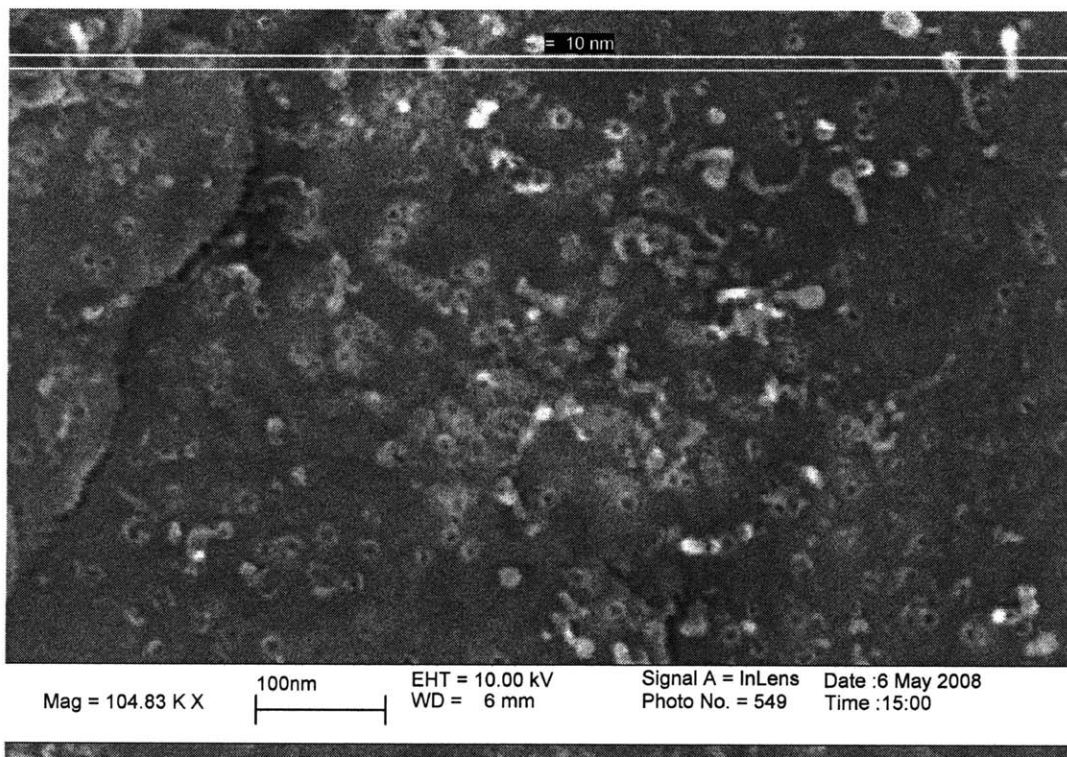
Figure 2.6: HR-SEM image of Tungsten substrate showing holes left after removal of CNTs by sonication. Small circles indicate location of removed nanotubes Density is estimated as 5×10 cm^{-2} (212 holes/ [834 x 506 nm]). Image taken on Raith 150 by R. Signorelli, X. Ji, and D. Ku.

3 Current Collector

Different materials used as a substrate for growing CNT arrays are described. We have progressed from semi-conducting substrates such as silicon, to metal substrates, and finally to metal foil substrates. This is essential because of the need of a thin, highly conductive current collector as part of the electrode. The importance of the substrate's surface smoothness is discussed and CNT growth results on the various substrate materials are presented.

3.1 Choice of Conducting Substrate

3.1.1 Transition from Silicon substrate to conducting substrate

A variety of different conducting materials have been used as the substrate for nanotube growth, including tungsten and aluminum. As previously noted, initial CNT growth experiments were performed on silicon (Si) substrates deposited with an underlayer and catalyst layer. These silicon substrate samples were used as a baseline against which other substrate materials were compared.
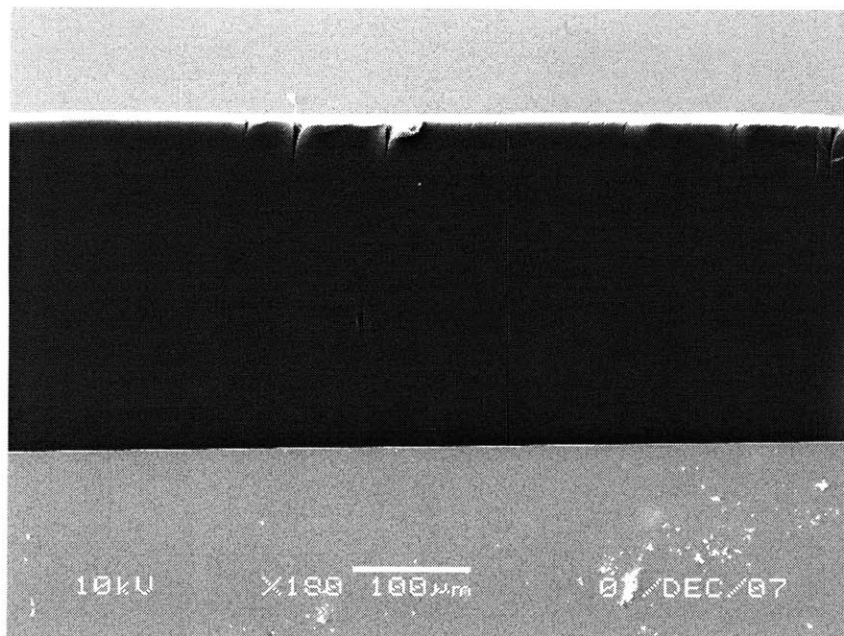
Figure 3.1: SEM image of CNT array grown on Si substrate with Al_2O_3 (15 nm) underlayer and Fe (1.5 nm) catalyst. CNTs have a height of 250μm.

Figure 3.1 is an SEM image that shows the dense array of CNTs that are capable of being grown on Si wafers. The CNTs also achieve a height of 250 μm during the 30 min. growth period. Achieving a robust growth of CNTs on Si wafers verified that the LP-CVD setup was functional and capable of growing vertically aligned arrays of CNTs. SEM images were produced on a JEOL 5910. The samples to be imaged are mounted on vertical holders in order to take profile images that reveal height data.

Tungsten was then selected as the conducting substrate for growth of CNT-based electrodes. Tungsten has a high melting temperature (3422° C) capable of withstanding the high temperature CVD process, as well as a relatively low electrical resistivity (5.5 μΩ·cm).

Tungsten (W) wafers (99.9% pure, Alfa Aesar) that are 500 μm thick, 50 mm wide, and 100 mm long were cut into 1 cm x 1 cm samples by a diamond saw. After deposition of underlayer and catalyst, the attempts to grow CNTs on these substrates yielded less robust results that silicon substrates, as seen in Figure 3.2. Height of the CNT array is only ~25 μm.
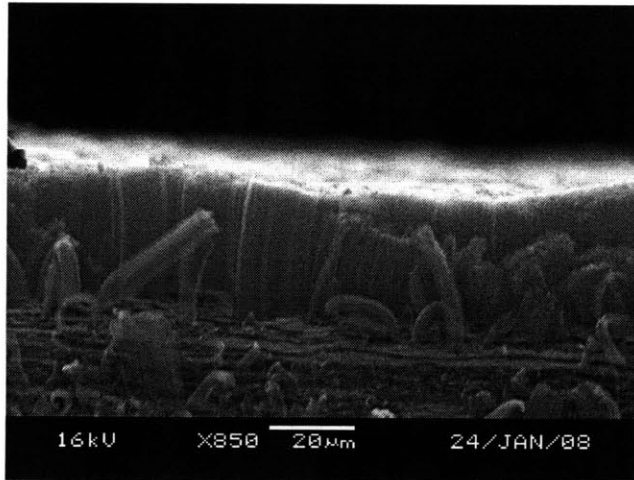
Figure 3.2: SEM image of CNTs on Tungsten substrate. The CNT array is much less uniform and visibly less dense when compared to growth on a Si substrate.
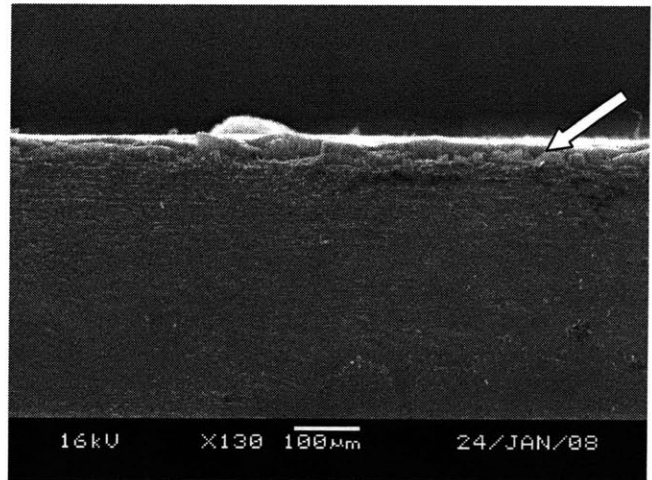
Figure 3.3: SEM image of Tungsten substrate showing flaring of edges where substrate was cut by diamond saw.

The SEM images in Figure 3.2 and Figure 3.3 also reveal several difficulties with regards to imaging when dealing with tungsten substrates. First, the interface between the W substrate and CNT layer is blurred by the flaring of the edges of the W substrate due to the diamond saw dicing. As a result, a procedure was established in which multiple passes of increasing depth were used to slowly cut the substrate and prevent flaring. Second, because the sample is cut before the deposition step, there are often catalyst nanoparticles in the cut grooves between each 1 cm^2 sample. These nanoparticles also yield CNTs during the growth process, which frequently block the view of the bulk CNT array.

3.1.2 Surface Morphology

The degraded growth on thick tungsten substrates led to significant investigation into surface morphology of substrate materials.

3.1.2.1 Atomic Force Microscopy

Because of the silicon substrate's higher yield, it was hypothesized that the surface roughness of substrate was correlated with CNT growth. Atomic force microscopy (AFM) was used to examine the differences in morphology between the tungsten substrates and silicon substrates. Tapping-mode AFM uses a cantilever tip, typically made of silicon and with a radius of curvature on the order of nanometers, which is raster scanned across the surface of a sample. The cantilever is oscillated at close to its resonant frequency by a piezoelectric driver. As the tip scans across the surface, it comes into intermittent contact with the sample. As the cantilever interacts with the sample's surface, its amplitude of oscillation changes. A feedback loop is used to maintain a constant oscillation amplitude and force on the sample. This data is used to obtain topographic data for the sample.

The AFM also allows for phase imaging, which is capable of showing differences in composition, adhesion, and various other properties. Phase data is collected by comparing the phase lag of the cantilever oscillation relative to the piezoelectric driver. Phase images are often hard to interpret, but they are usually used to highlight edges in the sample. When compared to topographic data, they can reveal edge boundaries that are often lost in rough topography.

The AFM images presented in this thesis show both the topographic image (right side) and phase data (left side). The data scale for each image is given below the image. Lighter colors represent values higher on the scale, and darker colors represent values lower on the scale.

3.1.2.2 Surface Roughness

AFM topographic data for a thick tungsten substrate and a silicon substrate with deposited underlayer and catalyst are shown in Figure 3.4 and Figure 3.5, respectively. As postulated, the topographic data shows that the tungsten substrate is much rougher than the silicon substrate; surface features are >3 μm in the tungsten substrate, while surface features are <5 nm on the silicon substrate.
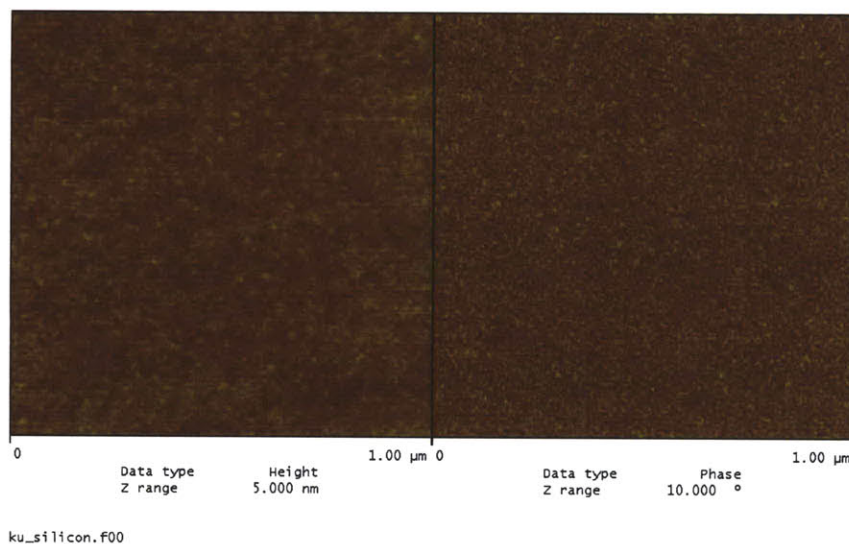
Figure 3.4: Silicon substrate. Manufacturer polished silicon substrates have surface features with size less than 5nm. Left image shows topographic data and right image shows phase data.

0		1.00 μm 0		1.00 μm
Data type	Height	Data type	Phase	
Z range	5.000 nm	Z range	10.000 °	

ku_silicon.f00
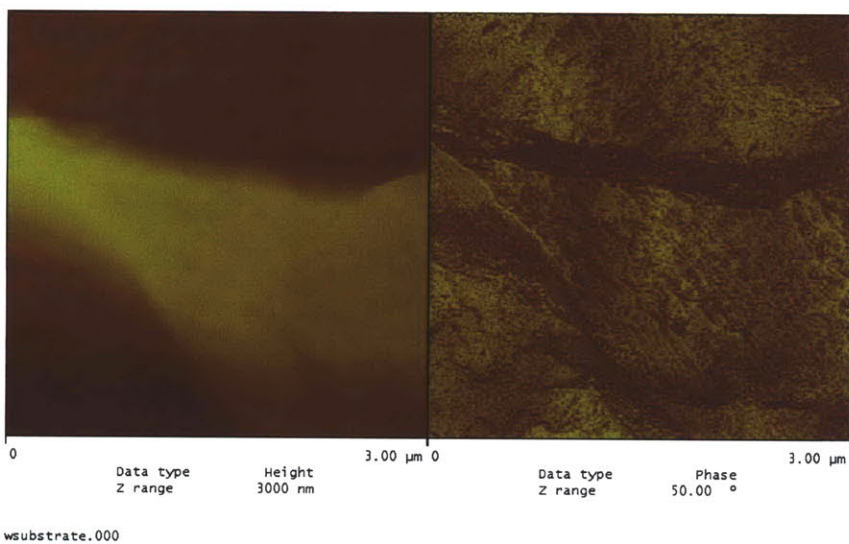
Figure 3.5: Unpolished Tungsten Substrate (500 μm thick). Left side topographic data shows 3 μm feature size.

0		3.00 μm 0		3.00 μm
Data type	Height	Data type	Phase	
Z range	3000 nm	Z range	50.00 °	

wsubstrate.000

As a result of surface roughness, the deposited catalyst nanoparticles are lost in the surface features of the tungsten substrate. Figure 3.6 shows the catalyst nanoparticles deposited onto a thick tungsten substrate. When compared to a silicon substrate, as shown in Figure 3.7, the catalyst nanoparticles are much less defined. Therefore, a smoother surface on a tungsten substrate that allows for more defined catalyst nanoparticle formation is necessary for greater CNT yield.
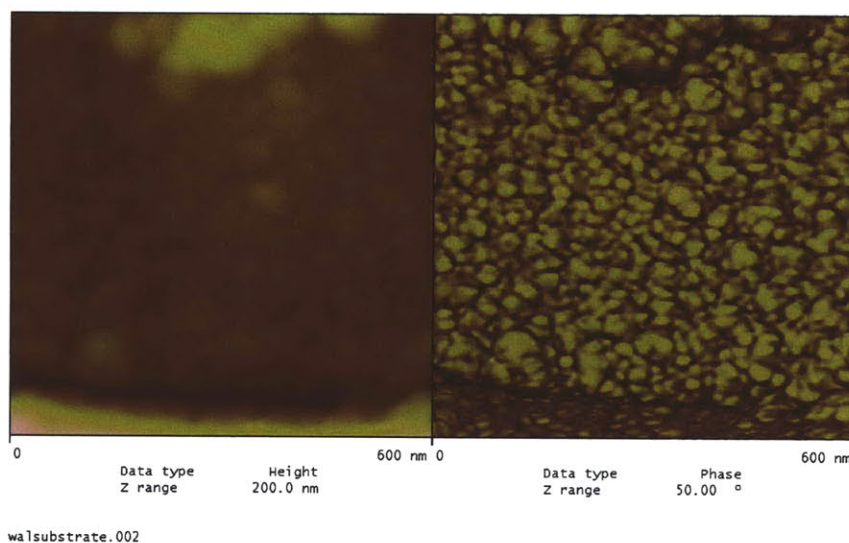
Figure 3.6: AFM image of thick W sample w/ 15 nm Al and 1.5 nm Fe. The image on the left is topographic data and the image on the right is phase data. The catalyst nanoparticles are lost in the surface roughness of the sample (note the 200 nm height scale).
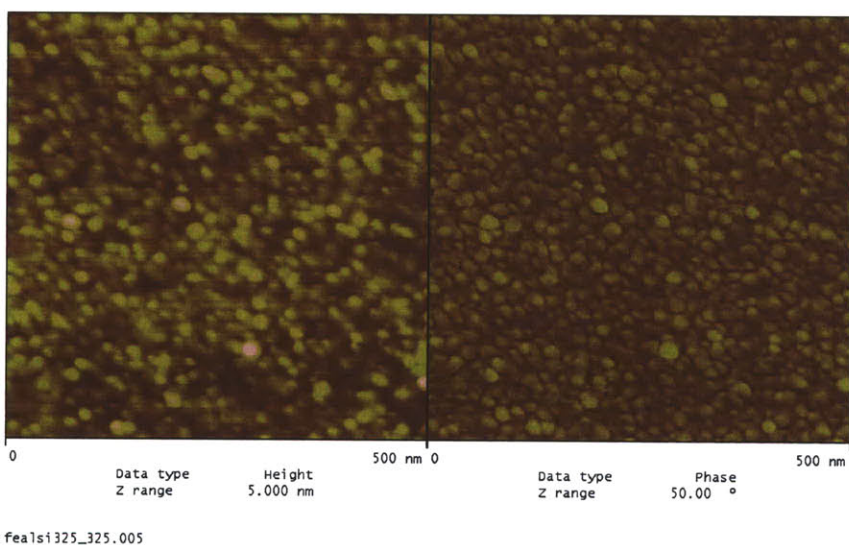
Figure 3.7: AFM image of Si sample w/ 15 nm Al and 1.5 nm of Fe. The image on the left is topographic data and the image on the right is phase data. The catalyst nanoparticles are clearly defined (5 nm scale).

3.1.2.3 Polishing Techniques

Two different techniques were used to polish the tungsten substrate for a smoother surface. A mechanical sandpaper polish technique was attempted; however, this failed to sufficiently smooth the surface. The process also left large visible scratches

41

across the substrate surface due to the nature of sandpaper polishing. A chemical-mechanical polishing (CMP) procedure (performed by Skip Hoyt, Lincoln Laboratory) was then used. AFM topography data for the CMP polished tungsten is shown in Figure 3.8. As polished, the AFM image shows large residue deposits from the CMP process. The substrates were therefore thoroughly cleaned using methanol to eliminate the residue, as shown in Figure 3.9). The topographic data shows a reduction in feature sizes from 3 μm to 50 nm for the CMP process.

Data type	Height	
Z range	50.00 nm	

Data type	Phase	
Z range	50.00 °	
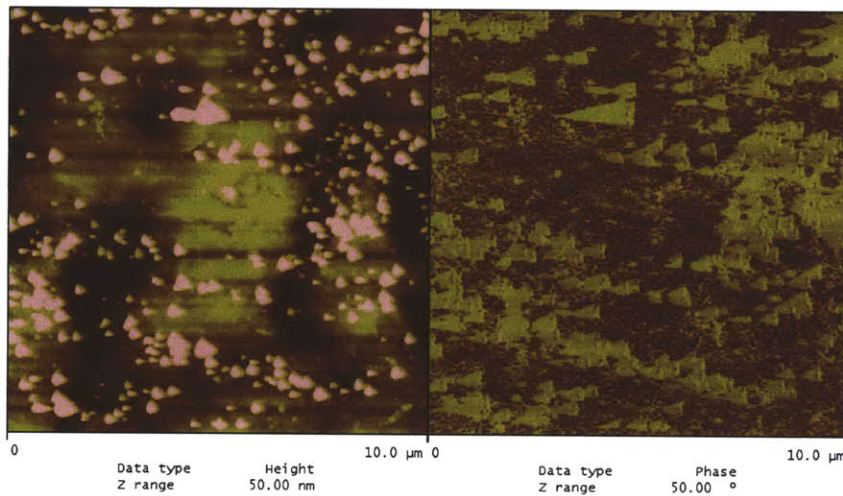
cmp_w.f02

Figure 3.8: CMP polished Tungsten Substrate (500 μm thick). Left side topographic data shows 50 nm feature size. Large clumps are residue remains from CMP process.
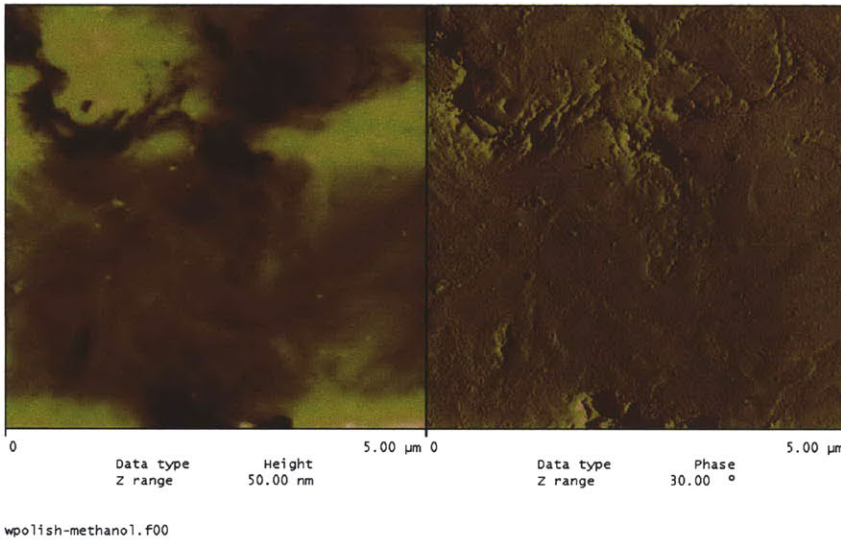
Figure 3.9: CMP polished Tungsten Substrate (500 μm thick) after cleaning with methanol. Residue remains have been eliminated.

wpolish-methanol.f00

3.1.3 Growth on Polished Tungsten Substrate

After CMP polishing and rinsing the tungsten substrate with methanol, an underlayer (15 nm aluminum) and catalyst layer (1.5 nm iron) were deposited using electron beam deposition. Using the OAG process, we were able to synthesize significantly improved CNT arrays of ~80 μm length with a CNT weight of approximately 0.5 mg, as shown in Figure 3.10. The density of the CNT array is on the order of 5×10^{10} cm^{-2}.
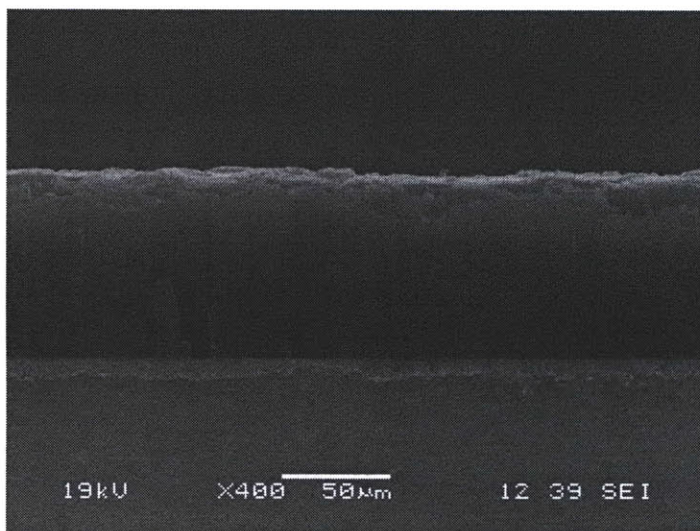
Figure 3.10: SEM Image of CNT growth on CMP polished tungsten substrate. The image is taken as a profile shot of the edge of the substrate. Height of CNT array is ~80 μm. (Sample 082008-2)

Although the tungsten substrates did not achieve the targets shown in Table 6.1, they demonstrate that a vertical array of CNTs can be grown directly on a conducting substrate. To improve our results, we needed to move to a thinner and smoother conducting substrate. Also, at 500 μm thick, the tungsten substrate was too thick to roll into an electrode. The thickness of the electrode also increases its thermal mass, which may prevent the substrate from heating as quickly as desired in the growth process.

3.1.4 Foil Substrates

3.1.4.1 Tungsten Foil

Tungsten foil substrates (50 μm thick, Alfa Aesar, 99.95% metals basis) were the next material used as the current collector for CNT growth. In comparison to the thick tungsten substrates, the tungsten foil is 1/10 as thick and much smoother due to the rolling process used for creating foil. AFM imaging of the surface topography as seen in Figure 3.11 shows a much smoother surface with features <50 nm in height. A large amount of the roughness can be attributed to the roller marks caused when creating the foil. Figure 3.12 is an AFM image of the tungsten foil substrate after deposition of 15 nm Al and 1.5 nm Fe. The catalyst nanoparticles are distinct and well-formed.

44
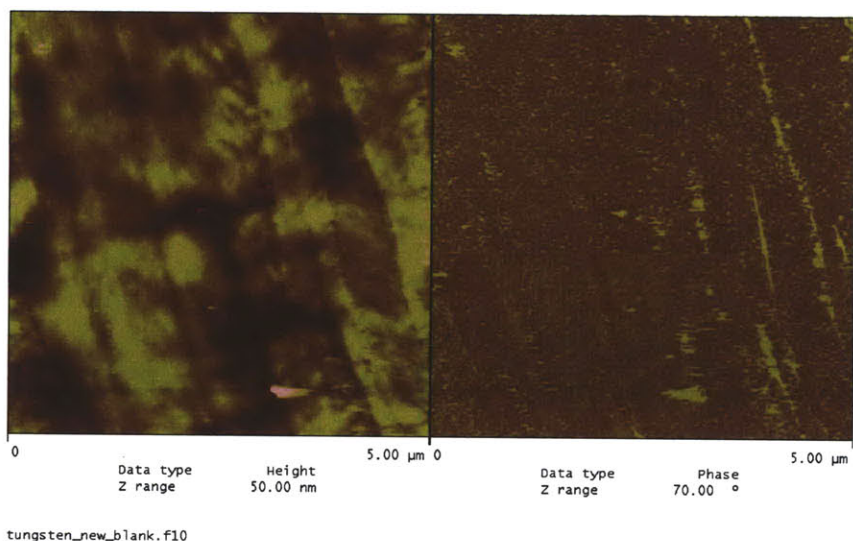
Figure 3.11: AFM image of Tungsten foil substrate. Left image of surface topography shows roller marks from the foil-making process. Surface features are <50 nm.
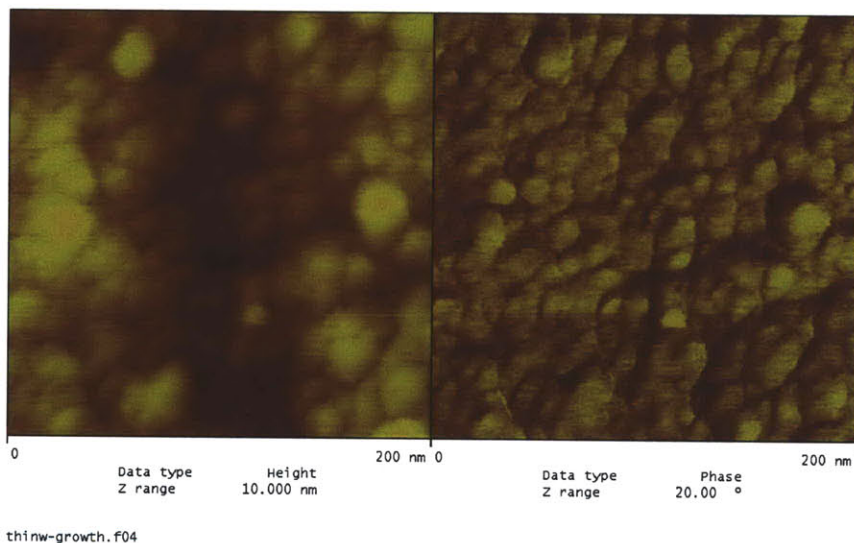
Figure 3.12: AFM of Tungsten foil substrate after deposition of underlayer and catalyst. Catalyst nanoparticles are well-formed and not lost in surface features. Nanoparticles are from 25 nm-30 nm in diameter.

OAG process CNT growth on the tungsten foil substrates yielded very promising results. For 30 min of growth, CNT array weight of 1.0 mg and height of ~100 μm were achieved. SEM images of growth on tungsten foil are shown in Figure 3.13 and Figure 3.14. Because the samples were cut in 1 cm² squares with a die saw before deposition,

flaring of the edges and extraneous growth are again evident at the front edges of the images.
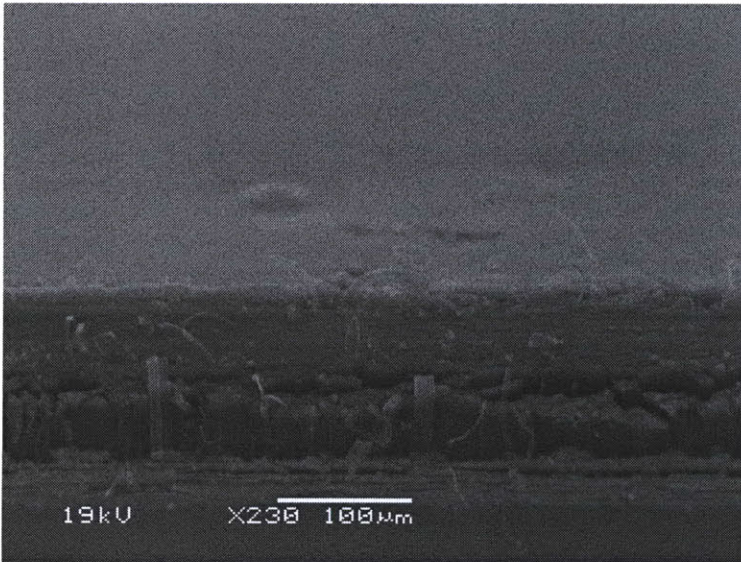
Figure 3.13: SEM image of CNT growth of Tungsten foil. This image is tilted at 10° to view the top surface of the CNT array. (Sample 111908-1)
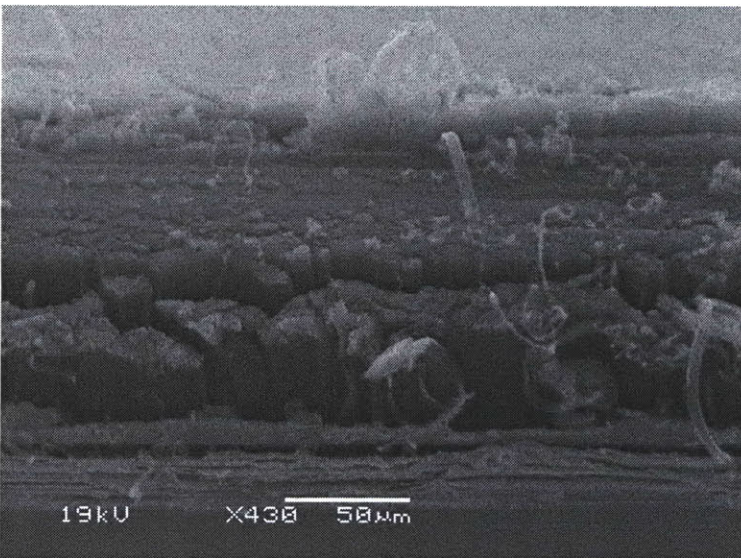
Figure 3.14: SEM image of CNT growth of Tungsten foil. It is difficult to see where the interface between foil and CNT is located, but assuming a 50 μm foil thickness gives a CNT array height of ~120 μm. (Sample 111908-1)

Although promising CNT growth was achieved on tungsten foils, tungsten is not an ideal material for use as a current collector because of its high cost. The tungsten foil experiments have demonstrated that CNT growth is realizable on thin conducting foils; however, a cheaper substrate material is necessary for future manufacturing considerations.

3.1.4.2 Aluminum Foil

Aluminum foil is produced in large quantities for a variety of purposes. Because it is cheap, plentiful, flexible, and conducting, it is an ideal substrate for use as a current collector in an electrode.

The aluminum foil used in these experiments was common household 'kitchen foil' (Reynold's Wrap Extra Heavy Duty). The aluminum foil was rinsed with methanol to remove any contaminants. Due to its production process, aluminum foil has a shiny side and a matte side. For our experiments, deposition was performed on the shiny side.

The thickness of the aluminum foil was ~30 µm. Aluminum foil samples were cut into 1 cm^2 samples by hand using scissors and care was taken to avoid bending the foil. The aluminum foil was very difficult to handle in comparison to other substrate materials because of its thinness, flexibility, and low weight.

AFM imaging of the aluminum foil revealed a smooth surface with minimal surface features (<30µm), as seen in Figure 3.15. An AFM image of the aluminum foil after deposition of an underlayer (15 nm Al) and catalyst layer (1.5 nm Fe) is shown in Figure 3.16. Catalyst nanoparticle density on the aluminum foil is estimated to be 4 x 10^{11} cm^{-2}.

0		1.00 µm 0		1.00 µm
	Data type	Height	Data type	Phase
	Z range	30.00 nm	Z range	50.00 °

al_foilf.000
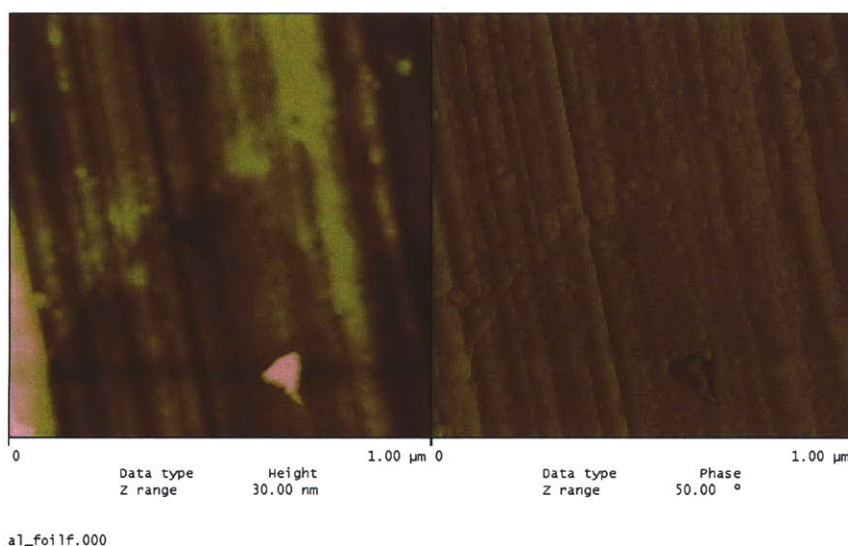
Figure 3.15: AFM image of aluminum foil. Topography shows features <30 µm. Roller marks are again evident due to the process of creating foils. Large particle in lower part of image is a dust particle.
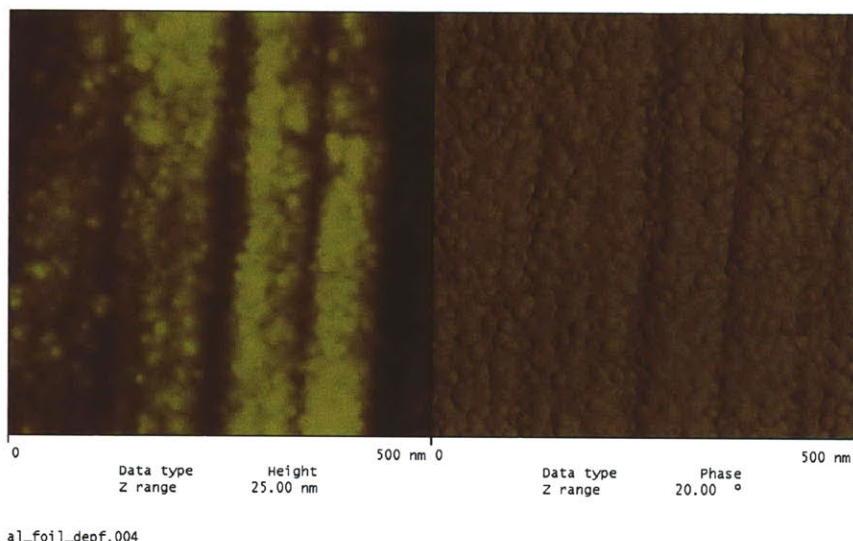
Figure 3.16: AFM image of aluminum foil with 15nm Al and 1.5 nm Fe deposited. The density of catalyst nanoparticles is ~5 x 10^{11} cm^{-2}

al_foil_depf.004

A major advancement in the direct growth of CNTs on a conducting current collector was achieved by successfully synthesizing CNT arrays of ~80 μm and weighing 0.9 mg. Sample SEM images are shown in Figure 3.17 and Figure 3.18. As previously mentioned, the flexibility of the aluminum foil makes handling the sample very difficult, and as a result, SEM imaging is ultimately a destructive process for the aluminum foil samples.
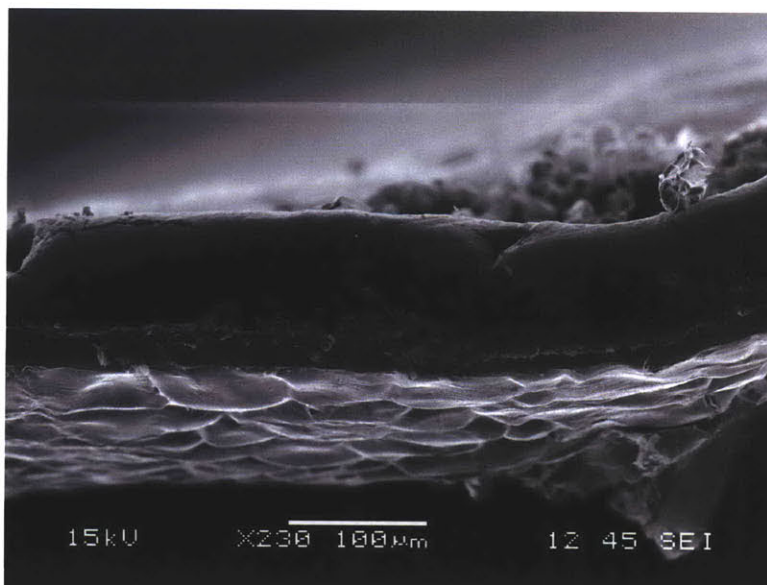
Figure 3.17: SEM image of CNT growth on aluminum foil. (Sample 090408-1)
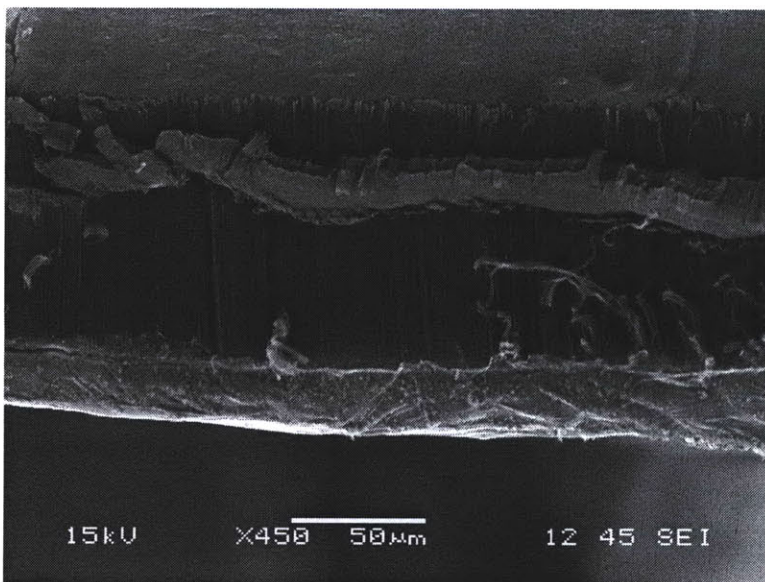
Figure 3.18: SEM image of CNT growth on aluminum foil (Sample 090408-1)

3.2 Summary of Growth Results on Different Substrates

Successful growth of a vertically aligned CNT array on a variety of different conducting substrates was achieved. We have found that surface smoothness is crucial to successful growth; without a smooth surface, the formation of catalyst nanoparticles is obscured and results in poor CNT growth. A summary of the growth results based on substrate material is shown in Table 3.1.

Table 3.1: Summary of Growth Results on Various Substrates

Substrate Material	Substrate Thickness	Smoothness (feature size)	CNT Array Thickness	Estimated CNT Density (CNTs/cm^2)
Silicon	600 μm	<5 nm	>250 μm	10^{12}
Tungsten	500 μm	3 μm	<20 μm	10^{10}
CMP Polished Tungsten	500 μm	50 nm	80 μm	5×10^{10}
Tungsten Foil	50 μm	<50 nm	100 μm	10^{11}
Aluminum Foil	30 μm	<30 nm	80 μm	3×10^{11}

The values shown in Table 3.1 are our best repeatable results for 30 minutes of growth using the OAG process. A clear progression of increasing density can be seen with decreasing feature size. However, our results show that a smooth substrate is still not enough to achieve our goal density of 10^{12} CNTs/cm^2. As a result, other factors such as catalyst layer thickness and variations in growth methods must be examined.

4 Parametric Optimization

Because CNT growth depends on many parameters, considerable time was taken to evaluate a number of dependencies. The first two sections of this chapter analyze the choice of material(s) for the catalyst and the thickness of the catalyst layer. The role of the underlayer is then examined. As previously discussed in Section 2.3, the LP-CVD growth system also allows for control of a wide variety of parameters, including the gas profile and the temperature ramp profile. The gas profile control allows for changes in flow rate for each type of gas during the growth period. Similarly, temperature profile control allows for variations in how fast the temperature is ramped up to the set growth temperature. The affect of a varying hydrogen profile and varying temperature ramp profile on CNT growth was explored.

4.1 Choice of Catalyst

In the CVD process, CNTs are formed by the decomposition of a carbon-containing precursor over a metal nanoparticle [29]. The nanoparticles are typically transition metals such as Ni, Co, or Fe, which act to catalyze CNT growth. These materials are able to decompose carbon compounds, form metastable carbides, and allow for the possibility of carbon atoms to diffuse over and through their surface very quickly.

Although several materials are able to catalyze CNT growth, iron catalysts are reported to be the most active of the tested transition metals, yielding the most dense and robust growth [30][31][32]. For this reason, most of our work was performing using an iron catalyst layer. However, alternatives to iron were also explored.

While iron is regarded as the most active of the three traditional catalyst metals, growth experiments were also performed using palladium (Pd) as the catalyst. Palladium is a transition metal that is part of the platinum family and belongs to the same group as

51

nickel in the periodic table. Palladium was selected as a possible catalyst material because unlike iron, it does not oxidize in air and would thereby decrease contact resistances in an ultracapacitor electrode. Palladium (2 nm) was deposited on silicon substrates with an aluminum oxide (15 nm) underlayer. However, these samples did not yield any CNT growth, but instead resulted in large carbon nanofiber formation. No further experiments were attempted using palladium as a catalyst layer.

The use of multiple catalysts may improve CNT growth length and density. The addition of a small amount of molybdenum (Mo) to Fe has been shown to increase catalytic activity[33][34]. This synergistic relationship may be due to the fact that one metal is responsible for nucleation, while the other is responsible for growth and defect repair [35].

A bi-metallic catalyst using a combination of iron and molybdenum was also evaluated as a possible method to increase density and improve CNT length. Silicon substrates were deposited with 15 nm of aluminum oxide, 1.5 nm of iron, and 0.3 nm of molybdenum, which were similar to the experimental conditions of Hart et al [34]. The e-beam deposition of molybdenum proved to be very difficult, as full power on the e-beam yielded a very small and inconsistent deposition rate. As a result, more molybdenum may have been deposited than was actually measured. Our growth attempts on the bi-metallic catalyst samples were unsuccessful, as we were unable to even achieve nucleation on the samples. The same conditions were also attempted on aluminum foil with no success.

Previous work from other groups and our own failed experiments determined that iron would remain our catalyst of choice for dense CNT growth. Our focus in examining iron catalysts was the affect that the amount of deposited iron played on the density of CNT growth.

4.2 Catalyst Layer Thickness

In conjunction with the smoothness of the current collector, the thickness of the catalyst layer also plays a major role in the formation of catalyst nanoparticles. At the nanometer-level thickness of deposition, the deposited films are discontinuous and therefore coagulate into nanometer sized clusters. We have hypothesized that varying the thickness of the catalyst layer also varies the diameter of the catalyst nanoparticles. By decreasing the thickness of the deposited catalyst, we can create nanoparticles with smaller diameters and increase the density of the CNT array.

Continuously decreasing the thickness of the catalyst thin film will eventually result in a decrease in nanoparticle density as there is not enough deposited material to form the necessary nanoparticle clusters. An optimal thickness for the catalyst thin film layer will likely be found empirically, and may vary depending upon growth conditions. Currently, the electron beam evaporator that we are using is not capable of reliably detecting small ($\Delta<0.2$ nm) changes in thin film deposition. The e-beam is also not as reliable in measuring thinner layers of thin films (<0.5 nm).

4.2.1 Silicon Substrates

AFM images were taken of silicon substrates deposited with 1.5 nm of Fe and 1.0 nm of Fe. Both substrates also had a 15 nm underlayer of Al. Their AFM topography and phase images are shown in Figure 4.1 and Figure 4.2. For the substrate with 1.5 nm of Fe, the average catalyst nanoparticle diameter is 15-20 nm, while the substrate with 1.0 nm of Fe has smaller nanoparticles of average diameter between 10-15 nm.

0   1.00 μm   0   1.00 μm
       Data type   Height   Data type   Phase
       Z range   5.000 nm   Z range   10.00 °

ku_silicon_fe15.f00
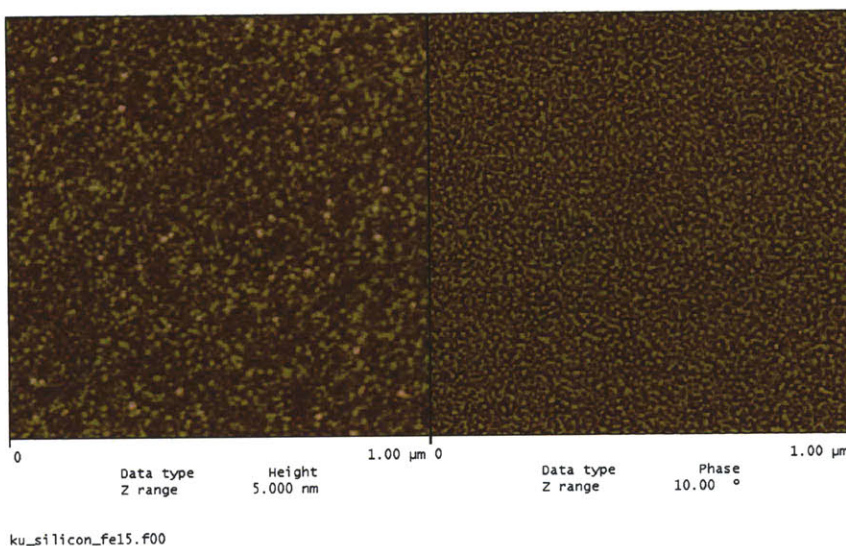
Figure 4.1: AFM image of silicon substrate with 15nm Al underlayer and 1.5 nm Fe catalyst layer. The average catalyst nanoparticle diameter is ~15-20 nm

0   1.00 μm   0   1.00 μm
       Data type   Height   Data type   Phase
       Z range   5.000 nm   Z range   10.00 °

ku_silicon_fe10.f02
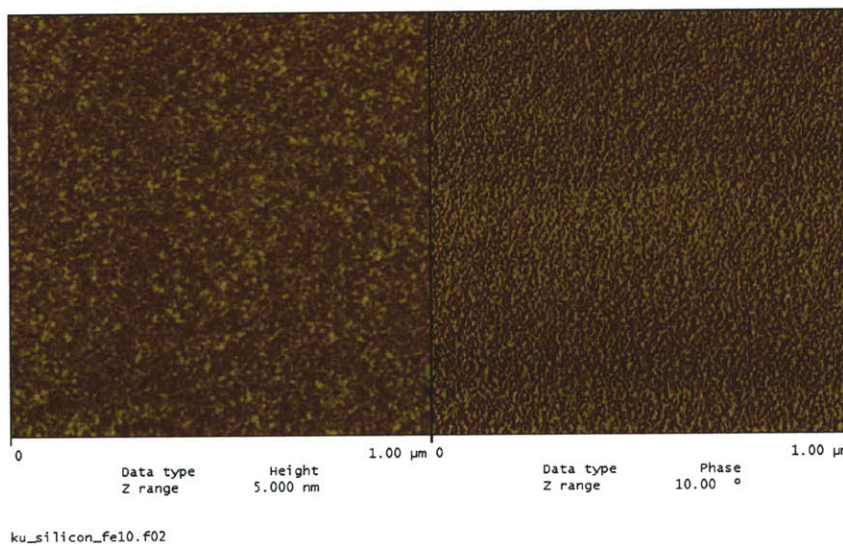
Figure 4.2: AFM image of silicon substrate with 15 nm Al underlayer and 1.0 nm Fe catalyst layer. The average catalyst nanoparticle diameter is ~10-15 nm

4.2.2 Tungsten Foil Substrates

AFM images of varying catalyst layer thicknesses were also examined on tungsten foil substrates. Figure 4.3 shows an AFM image of 1.0 nm of Fe deposited on tungsten foil with 15 nm of Al underlayer, while Figure 4.4 shows the same substrate and

underlayer with 1.8 nm of Fe. The 1.0 nm catalyst layer shows an average particle size of 25-30 nm, while the 1.8 nm catalyst layer shows an average particle size of 40-45 nm.
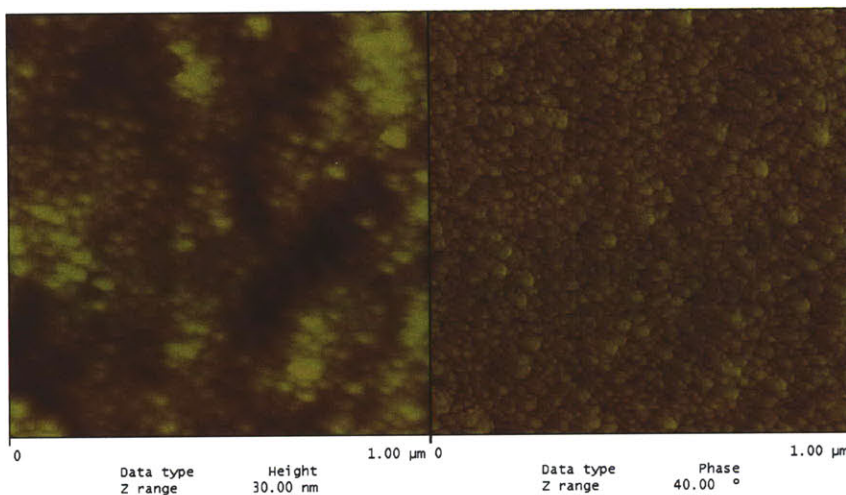
Figure 4.3: AFM image of tungsten foil substrate with 1.0 nm layer of Fe catalyst. Underlayer is 15 nm of Al. Average particle size is 25-30 nm.
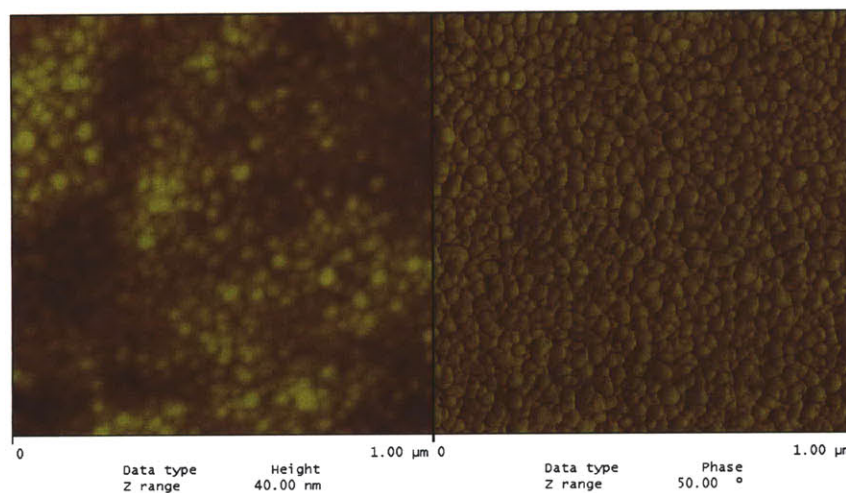
Figure 4.4: AFM image of tungsten foil susbtrate with 1.8 nm layer of Fe catalyst. Underlayer is 15 nm of Al. Average particle size is 40-45 nm.

A tungsten foil substrate with a 1.5 nm catalyst layer, as previously shown in Figure 3.12, also shows similar catalyst nanoparticle size distributions as the 1.0 nm layer (25-30 nm). Because the catalyst nanoparticles are not entirely uniform in size, it is

difficult to determine whether the nanoparticle density increases by decreasing the catalyst layer from 1.5 nm to 1.0 nm using AFM analysis techniques. Instead, nanotube density as measured by weight of CNT growth, may reveal a density increase. Even thinner catalyst layer depositions have not been attempted due to e-beam limitations.
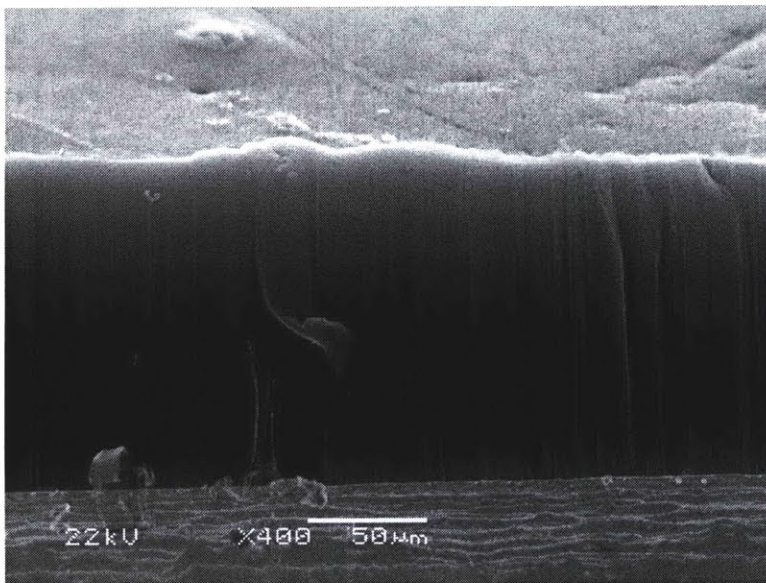
Figure 4.5: SEM image of CNT growth on tungsten foil with 15 nm of Al and 1.8 nm of Fe. (Sample 042709-3)
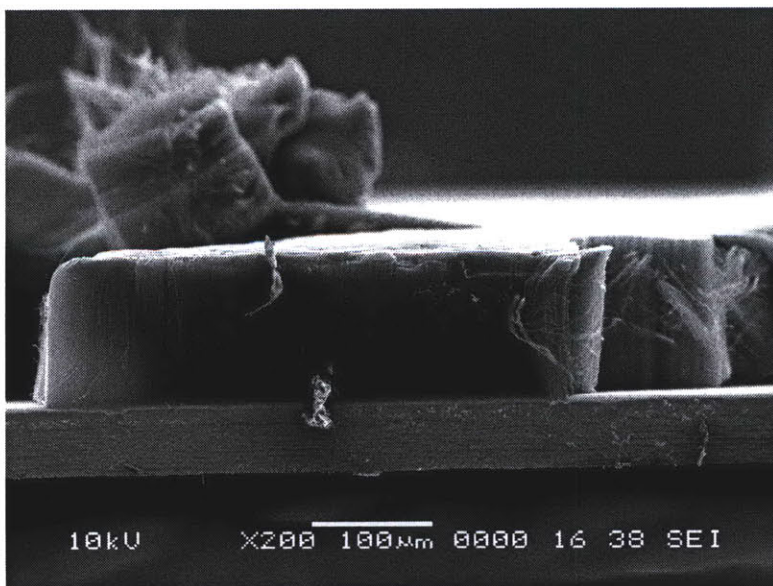
Figure 4.6: SEM image of CNT growth on tungsten foil with 15 nm of Al and 1.0 nm of Fe. (Sample 030309-1)

Table 4.1: Effect of Varying Catalyst Layer Thicknesses on CNT Growth

Catalyst Layer Thickness	Catalyst Nanoparticle Size (AFM)	CNT Thickness	CNT Layer Weight	Estimated CNT Density (CNTs/cm^2)
1.8 nm	40-45 nm	~100 μm	0.5 mg	5.4 x 10^{10}
1.5 nm	25-30 nm	~120 μm	1.0 mg	1.0 x 10^{11}
1.0 nm	25-30 nm	~120 μm	1.1 mg	1.1 x 10^{11}

As summarized in Table 4.1, our experiments have confirmed our hypothesis that decreasing the catalyst layer thickness produces smaller nanoparticles, which allow for denser nanotube growth. A more accurate system of depositing thin films would allow us to better optimize a catalyst layer thickness to maximize the nanoparticle density.

4.3 Underlayer

The support layer or underlayer of material between the substrate and catalyst layer performs an underappreciated role in the growth process. The underlayer prevents the substrate and catalyst layer from interacting and forming undesirable compounds that limit the availability of catalyst nanoparticles for nucleation and growth [5][2]. Therefore, in choosing an underlayer, the interactions between the catalyst layer and underlayer must also be considered. The combination of aluminum oxide (alumina, Al_2O_3) underlayer and iron catalyst layers has been found to be very successful in yielding the growth of vertically aligned CNT arrays on a variety of different metal substrates [2]. However, alumina is an insulator and therefore unsuitable for use in an ultracapacitor electrode.

For our ultracapacitor electrodes, aluminum was selected as a metal underlayer because of its relative similarity to alumina. Electrode samples with a conducting current collector were all deposited with aluminum underlayers (15 nm) to improve their electrochemical behavior compared to electrodes with alumina underlayers. However,

aluminum also has a much lower melting point (660° C) when compared to aluminum oxide (2054° C). The melting point of aluminum is below the growth temperature used on all substrate material types (except for aluminum foil). Although the CNT growth temperature is higher than the melting point of aluminum, it is unclear whether a thin film of aluminum behaves in the same manner as bulk aluminum [36].
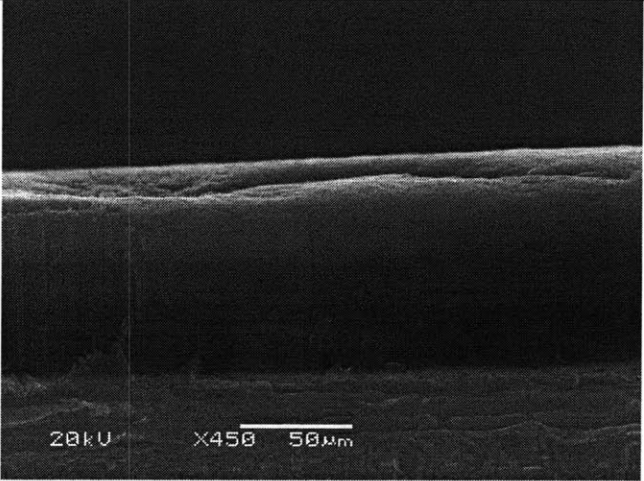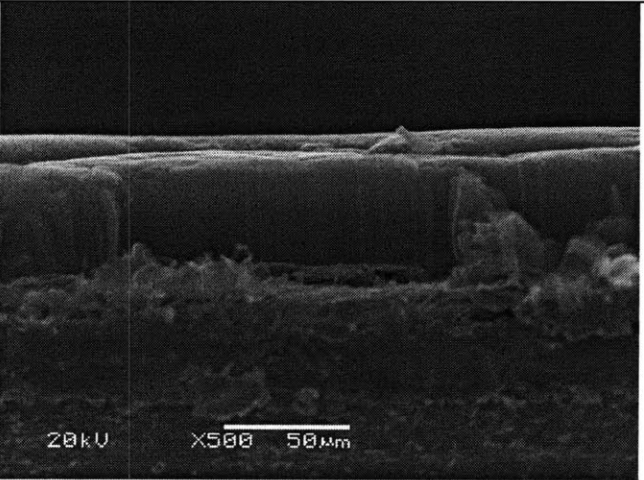
A melted underlayer of aluminum implies a liquid base in which catalyst nanoparticles are free to slide around and perhaps be gettered away from the surface. These unwanted surface interactions have caused some to question whether aluminum is a suitable underlayer for CNT growth [37]. However, because aluminum is very reactive, a thin layer (on the order of angstroms) of aluminum is oxidized to alumina in air. In using aluminum as the underlayer, it is nearly impossible to prevent a thin layer of alumina from forming. Our first step of oxidation in the growth process allows for oxidation of both the catalyst layer and underlayer. In forming an angstroms-thick layer of aluminum oxide, we may be preventing unwanted underlayer-catalyst interactions. The resulting morphology is complex and not fully understood, but growth results with this configuration have been encouraging.
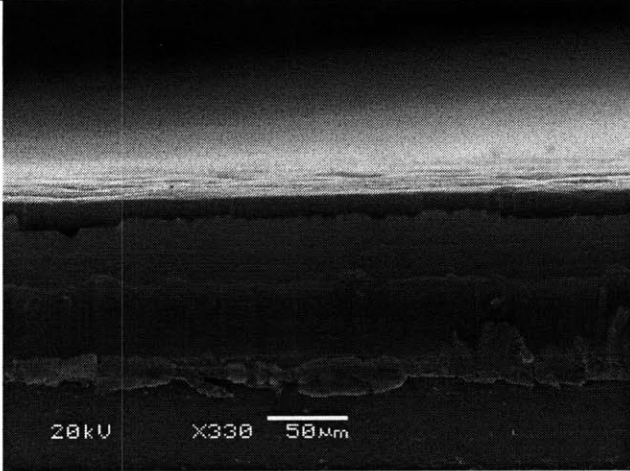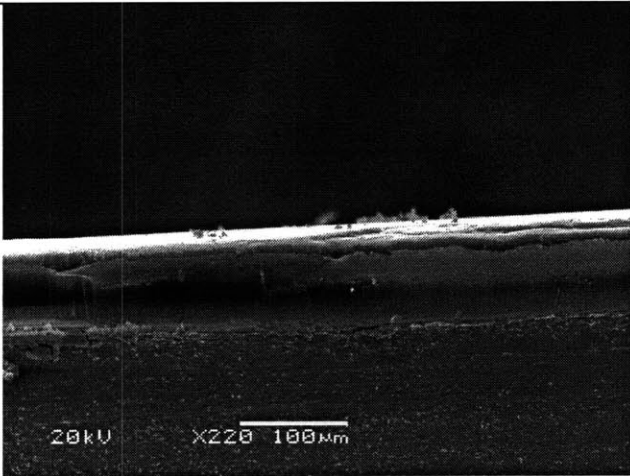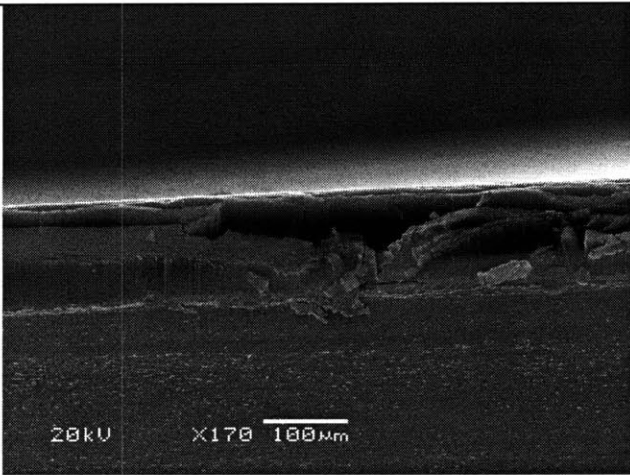
4.4 Varying Hydrogen Profile

The OAG growth process utilized a strict gas profile of 700 sccm of argon, 90 sccm of hydrogen, and 30 sccm of acetylene throughout the growth process. In this set-up, the argon flows provides most of mass for the deposition chamber pressure, while acetylene provides the hydrocarbons for CNT formation and growth. We hypothesize that the hydrogen acts as a reducing and etching agent for the catalyst nanoparticle. The hydrogen helps to slowly reduce the oxidized catalyst to metallic form and helps to etch away the buildup of amorphous carbon that eventually poisons the catalyst and halts the growth of CNTs. By delaying the hydrogen or introducing more hydrogen later in the growth process, a thicker array of CNTs may be produced.

A series of experiments with varying amounts of hydrogen during the growth step was performed. These experiments utilized a CMP polished tungsten wafer (500 μm thick, Alfa Aesar), as previously discussed, with 15 nm of aluminum as the underlayer, and 1.5 nm of iron as the catalyst layer. The experiments used the OAG process (30 min growth) with the following variations: (1) control experiment with constant H_2 during the growth step, (2) first half of growth period (15 min) without H_2 and second half with H_2, (3) first half with H_2 and second half without H_2, (4) decreasing the H_2 flow rate to by 10 sccm every three minutes (start at 90 sccm, final rate of 0 sccm), and (5) increasing the H_2 flow rate by 10 sccm every three minutes (start at 0 sccm, final rate of 90 sccm). The results of the experiments and representative SEM images are shown below in Table 4.2.

Table 4.2: Comparison of CNT Length with varying H_2 Profile

Hydrogen Gas Profile	Length (μm)	SEM Image (JEOL 5910)
Constant	~80	 **Figure 4.7:** 30 min CNT Growth on Thick W with constant H_2 profile (sample 032808-3)
1st Half: H_2 2nd Half: No H_2	~55	 **Figure 4.8:** 30 min CNT Growth on Thick W with H_2 in first 15 min only (sample 032108-1)

1st Half: No H_2 2nd Half: H_2	~60	 **Figure 4.9:** 30 min CNT Growth on Thick W with H_2 in second 15 min only (sample 032008-4)
Decreasing H_2 profile (-10 sccm/3 min from 90 sccm)	~80	 **Figure 4.10:** 30 min CNT Growth on Thick W with decreasing H_2 profile (sample 031808-2)
Increasing H_2 profile (+10 sccm/3 min to 90 sccm)	~90	 **Figure 4.11:** 30 min CNT Growth on Thick W with increasing H_2 profile (sample 032008-3)

The experiments support our hypothesis that hydrogen plays an important role in determining the length of the nanotube array. Decreasing the amount of time that hydrogen is allowed to flow by half, regardless of whether it is the first half or second half, severely limits the growth of CNTs. An increasing amount of hydrogen, as shown in the increasing profile, yielded the longest growth. This may be due to the fact that initially, because of the low flow rate of H_2, only a small amount of the catalyst nanoparticle is reduced to metallic form. CNTs are able to still able to nucleate, and as the amorphous carbon begins to build up, the increasing amount of H_2 is able to etch the amorphous carbon away, prolonging the growth. Although more rigorous experiments with a longer time scale may be needed to corroborate our findings, these results suggest that an increasing hydrogen profile may be optimal for producing long CNT arrays.

4.5 Varying Temperature Profile

During the OAG process, the oxidation and anneal step take place at relatively low temperatures (<400° C), while the growth step takes place at much higher temperatures. As shown in Table 2.1, the temperature ramp from the anneal step to the growth step is typically performed in two minutes. However, this slow ramp up in temperature means that the catalyst nanoparticles are subjected to increasingly high temperatures before nucleation occurs. At higher temperatures, the nanoparticles may have enough surface energy to move or coagulate into larger particles, decreasing the density of the array.

We have hypothesized that a faster temperature ramp will yield a denser array of nanotubes because the catalyst nanoparticles will not have time to rearrange at higher temperatures. Growth experiments were run in which we used a quick heat-up profile of just a few seconds. These set of experiments were not computer-controlled by the LabVIEW program temperature profile; instead, under manual control, a set amount of current that yields the necessary growth temperature is entered by hand and delivered by

the power supply after the anneal step. This allows a very quick temperature ramp of less than 10 seconds.

The CNT growth results of the quick heat-up procedure on tungsten foil substrates is shown in Figure 4.12 and Figure 4.13. The substrates contained an underlayer of 15 nm of Al, and a 1.5 nm Fe catalyst layer. SEM images show thickness in the range of 100 μm and the measured weight of the CNT array was as high as 1.3mg.
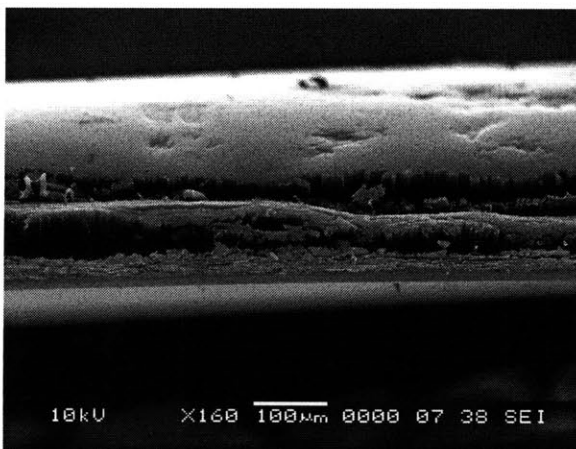
Figure 4.12: SEM image of CNTs on tungsten foil substrate using quick heat-up for growth. CNTs are approximately 100 μm in length. (Sample 021409-3)
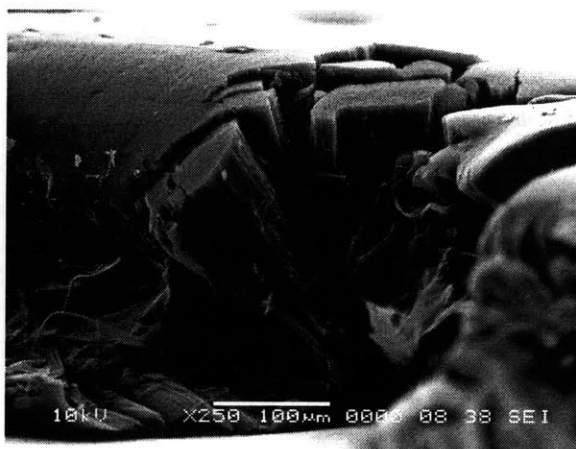
Figure 4.13: Close up SEM image of CNTs grown on tungsten foil substrate using quick heat-up procedure. (Sample 021409-3)

Compared to previous results of CNT growth on tungsten foil without the quick heat-up, the measured CNT weight increased by 0.2 mg while the CNT array height was the same. The weight increase without a height increase indicates a rise in the density of the CNT array, from 1×10^{11} CNTs/cm^2 to 1.4×10^{11} CNTs/cm^2.

5 Deposition Techniques

Up to this point, previous growth experiments utilized substrates with an underlayer and catalyst thin film deposited by electron beam deposition techniques. This chapter evaluates the use of sputter deposition as an alternative to electron beam deposition. Sputtering is more suitable for large-scale processes and manufacturing. A brief explanation of each technique is given, as well as a comparison of growth results.

5.1 Thin-Film Deposition Methods

The transition metals used for CNT growth need to be dispersed in order to properly catalyze growth. Bulk material is not suitable for growing large CNT arrays [38]. Instead, thin films are used as a way to prepare catalyst nanoparticles.

There are a variety of different techniques for growing thin films [5], including the sol-gel method [39], co-reduction of precursors [40], various precipitation methods[41][42], and various physical deposition methods [43][44]. These techniques vary widely in sophistication and in the quality of the film produced. Since our focus was on the deposition of pure metals, we relied on the physical deposition methods of electron beam deposition and sputtering. These two methods avoid the need to soak the substrate in solutions, preventing chances of contamination as well as allow for thin (nm) and evenly distributed films.

The majority of our prepared samples were created using electron beam evaporation (e-beam evaporation). E-beam evaporation allows for the deposition of a wide variety of both metals and dielectrics and can achieve very high deposition rates up to 100 Å/s. The low pressures utilized in e-beam evaporation also allow for a thin film of very high purity.

Sputtering techniques also allow for the deposition of a wide variety of metals and dielectrics. Sputtering operates under a lesser vacuum range than the e-beam; as a result, there is a higher chance of the introduction of impurities. However, sputtering is a more

appropriate choice for large-scale production, such as the manufacturing of a large electrode for commercial purposes. To achieve the best experimental results, the purity of e-beam evaporation is favored; however, sputtering was evaluated for its potential commercial applications.

5.1.1 Electron Beam Deposition

In e-beam evaporation, the substrate and source material are loaded into a deposition chamber. The chamber is pumped to a vacuum pressure of around 10^{-5} torr. The source material is then heated by an electron beam until the material reaches a vapor phase. When the vapor condenses, a solid coating is produced throughout the deposition chamber. The substrate is protected by a shutter, which is only open for a set amount of time, depending on the deposition requirements.

Deposition rate and the total amount of material deposited are measured by a piezo-electric, quartz crystal oscillator. The frequency of vibration of the crystal is altered by the amount of mass deposited, which allows for precise measurements.

E-beam deposition took place in MTL's EML facility using the Sloan 8kV e-beam. The electron beam is created by heating a tungsten filament using a high voltage power supply to 8kV. As the filament heats up, electrons are emitted. Since the electrons are emitted in a random fashion, a magnetic field is used to direct and accelerate the electrons into a beam pointed at the source material. The intensity of the beam is controlled by the current flowing through the filament.

In a typical deposition run, the chamber is pumped to a vacuum pressure of at least 2×10^{-5} Torr. For the aluminum layer, the filament current is gradually increased at a rate of 0.01 A/min until the deposition rate reaches 1.0 Å/s. Approximately 50 nm of aluminum is allowed to burn off to avoid contaminants before the shutter is opened for the deposition of a 15 nm layer. The iron layer is treated slightly differently. Iron has a tendency to "spit" when heated. Therefore, the filament current is increased at a rate of

0.005 A/min until the deposition rate reaches 0.2 Å/s. Approximately 10 nm of iron is burned off before depositing the iron thin film layer.

Figure 5.1 below is a picture of the e-beam evaporator used in our experiments. The large cylinder is the deposition chamber, which accounts for most of the size of the system. Figure 5.2 shows where the substrate is mounted inside the deposition chamber. The shutter and crystal oscillator can also be seen.
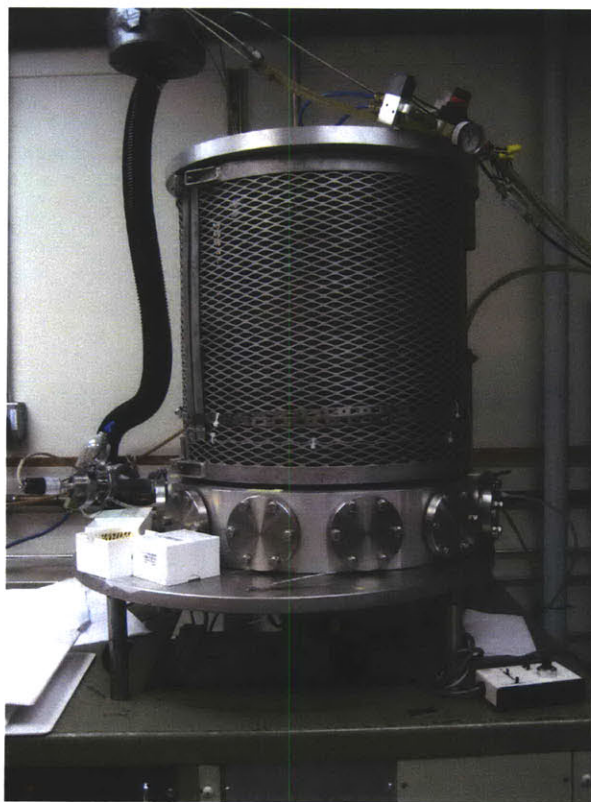
Figure 5.1: Sloan 8kV Electron Beam Evaporator used for deposition located at MIT in Exploratory Materials Laboratory (EML). The deposition chamber occupies most of the space in the system.
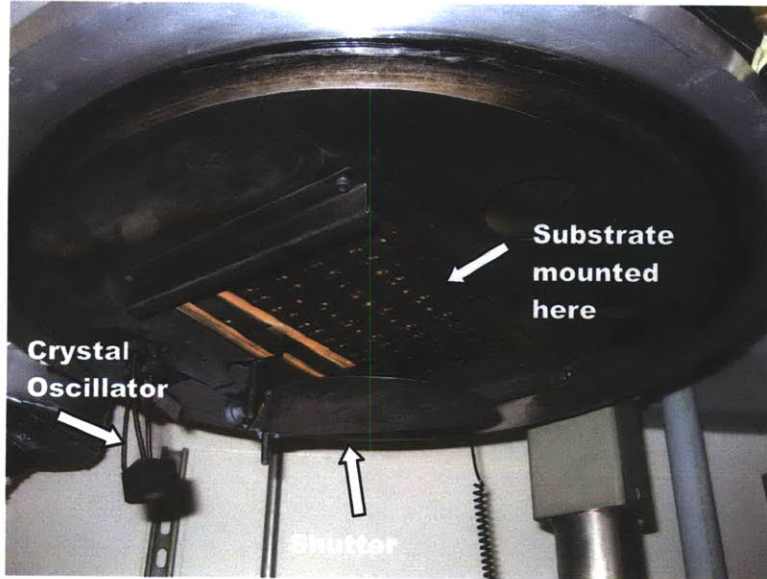
Figure 5.2: Inside the top of the deposition chamber. The substrate is mounted on a board that slides onto the mounts. The shutter shields the substrate until user is ready for deposition. The crystal oscillator measures the thickness of deposited layer.

For evaporation techniques, the mass deposition rate per unit area of source surface is governed by the Langmuire-Knudsen relation:

$$R_m = C_m \left(\frac{M}{T}\right)^{0.5} \cos\theta \cos\phi \left(\frac{1}{r^2}\right)(P_e(T) - P) \tag{5-1}$$

where M is the evaporant molecular mass (g), r is the distance from source to substrate (cm), T is the source temperature (K), $P_e(t)$ is the evaporant vapor pressure (which is a function of T, P is the chamber pressure (Torr), and C_m is a constant equal to 1.85×10^{-2} (K/Torr). The angles θ and ϕ are governed by the deposition geometry and are shown below in Figure 5.3.

The film deposition rate in terms of thickness is given by:

$$\frac{dh}{dt} = \frac{R_m A_e}{\rho} \tag{5-2}$$

where A_e is the source surface area (cm^2) and ρ is the source density (g/cm^3).
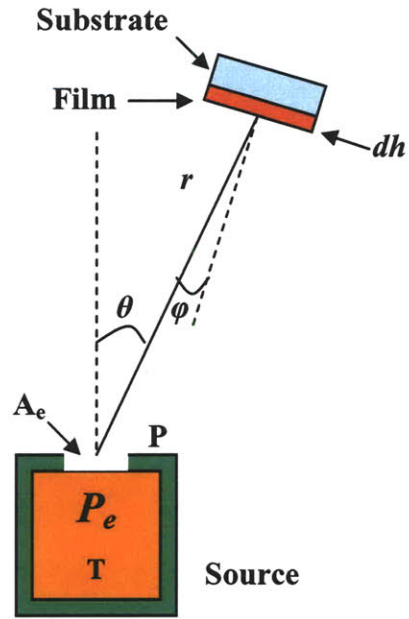
Figure 5.3: Deposition geometry and thickness rate

Since R_m is dependent upon the difference between evaporant vapor pressure and background pressure, the higher the evaporant vapor pressure and the lower the background pressure, the greater the deposition rate. The vapor pressure of different materials varies widely, leading to significantly different deposition rates for different materials. For compound sources containing several different elements, evaporation techniques often alter the stoichiometry of the material, yielding a thin film of different chemistry than the source material. The source material may either evaporate or sublime based on the melting point of the material and its vapor pressure.

The chemical purity of evaporated films depends on three factors: the purity of the source material, contamination from the crucible or other support materials, and the affect of residual gases present in the system.

5.1.2 Sputter Deposition

Sputtering is a process in which energetic ions from a gaseous plasma are accelerated at a source target. As the ions collide with the target, molecules are ejected or sputtered through energy transfer. These molecules are then deposited as they contact another material, such as the substrate. There are a variety of different types of sputtering techniques, including DC (direct current) sputtering and RF (radio frequency) sputtering.

In DC sputtering, the target (cathode) and substrate (anode) are placed in a neutral gas (typically argon) environment and charged by a DC power supply. The free electrons present in the deposition chamber are directed away from the cathode and impact the argon (Ar) atoms, causing them to lose an electron and turn into a positively charged ion. The Ar+ ions are then accelerated toward the negatively-charged target and the impact of the collision knocks free molecules from the target. The plasma appears to be glowing because a photon is released as free electrons recombine with argon ions. This process repeats continuously as long as the plasma is charged.

Magnets are often placed behind the target to improve the probability of the ionization of an argon atom by a free electron because the electrons are only able to travel in the path of the magnetic field. Magnetron sputtering allows for much higher deposition rates.

Dielectric materials cannot be deposited by DC sputtering because of charge buildup on the cathode. This is solved by alternating the potential of the target and substrate. At radio frequencies of <100kHz, the free electrons and ions are easily able to follow the switching of the anode and cathode. The process is basically the DC sputtering of both sides; the large electrode of the substrate and deposition chamber allow for very little sputtered material in that direction. RF sputtering allows for lower gas pressures and makes it easier to maintain a plasma.

The sputter method allows for high chemical purity in the deposited film. Since molecules are physically dislodged from the target, the sputtered target will maintain is stoichiometric ratios.

Sputtering was performed in MTL's EML laboratory, using the AJA International Orion 5 UHV, shown in Figure 5.1 below. The Orion sputterer is capable of handling one

DC target and two RF targets, as shown in Figure 5.5. Aluminum was deposited using RF sputtering at a rate of 1.0 Å/s. Due to its ferromagnetic properties, Iron was deposited using magnetron DC sputtering at a rate of 0.5 Å/s. Deposition rates were again calculated using a quartz crystal oscillator during a dummy run.
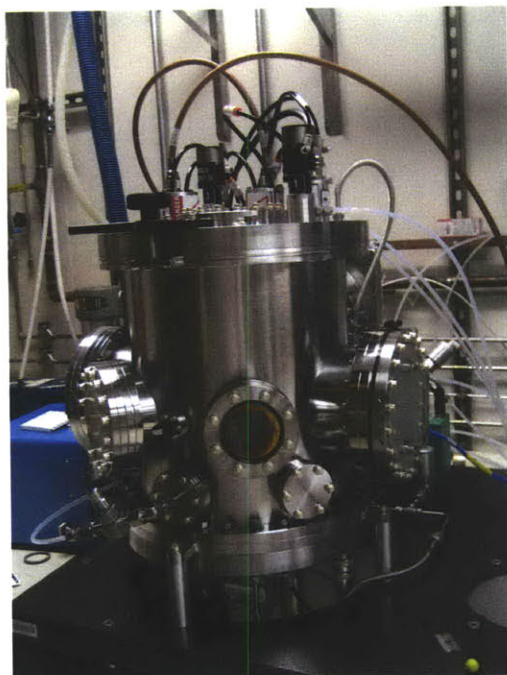
Figure 5.4: AJA International Orion 5 UHV Sputter Deposition System in the MTL's EML laboratory.
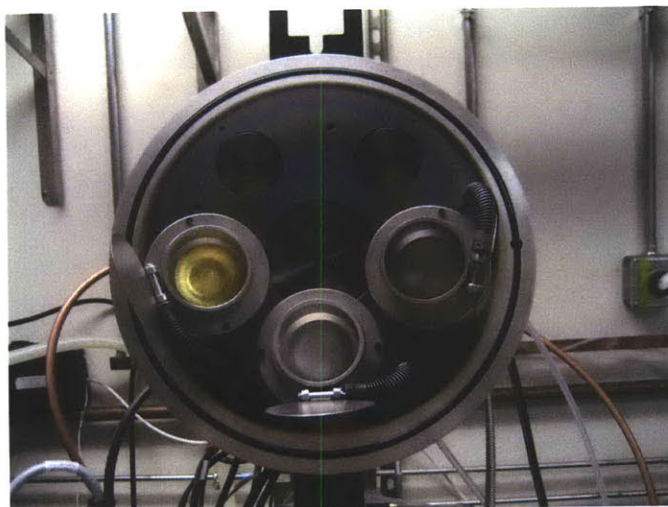
Figure 5.5: Inside the lid of the sputtering system. The system can hold three targets, which are shown with their shutters open. The target on the far right is used for DC sputtering.
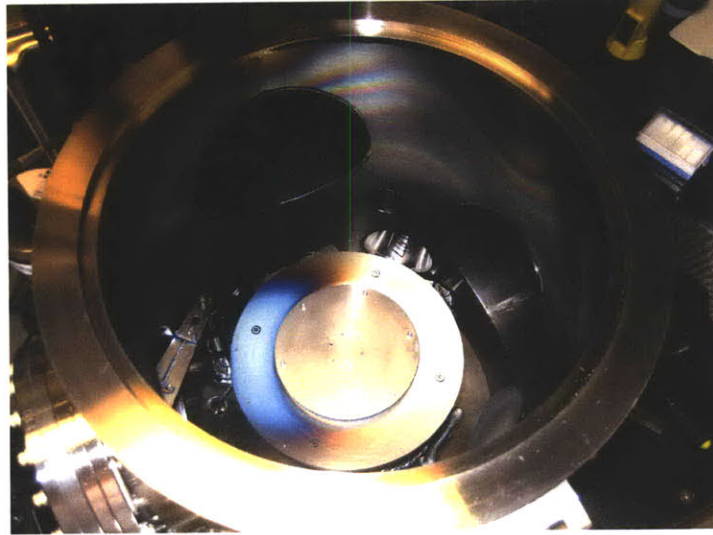
Figure 5.6: Inside the deposition chamber of the sputterer. The substrate is mounted on the chuck and spins during the deposition run to improve uniformity.

The inside of the sputter deposition chamber is shown above in Figure 5.6 . The substrate is mounted on the chuck, which is spun during deposition to insure uniformity.

5.1.3 Comparison of Growth Results

A tungsten foil substrates was sputter deposited with 15 nm of Al underlayer and a 1.5 nm Fe catalyst layer to compare with previous e-beam deposited samples. Although some minor variations in growth were expected by moving from e-beam to sputter deposition, we did not expect to encounter significant difficulties in achieving good growth. However, growth experiments on sputtered samples were disappointing.

CNT growth on sputtered substrates revealed very uneven thicknesses, as seen in Figure 5.7 and Figure 5.8. To the naked eye, the CNT array was visibly less dense for sputtered substrates. Although the SEM images show CNT thicknesses in excess of 100 µm, such growth was not uniform throughout the sample; the SEM only allows for profile imaging of the edges of the samples.
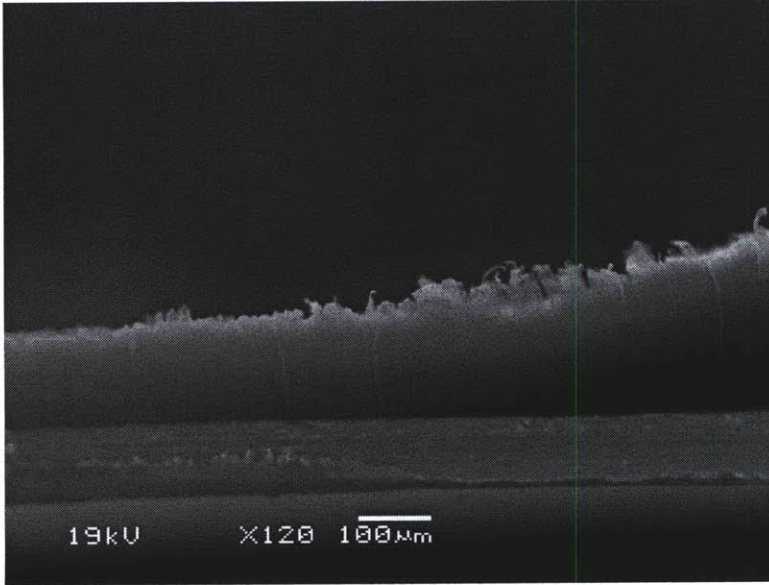
Figure 5.7: SEM image of CNTs grown on tungsten foil that was sputtered with 15 nm of Al and 1.5 nm of Fe. The CNT array height is uneven and variable. Despite thicknesses > 100 μm, the measured weight of the CNTs was only 0.3 mg, suggesting very low density.
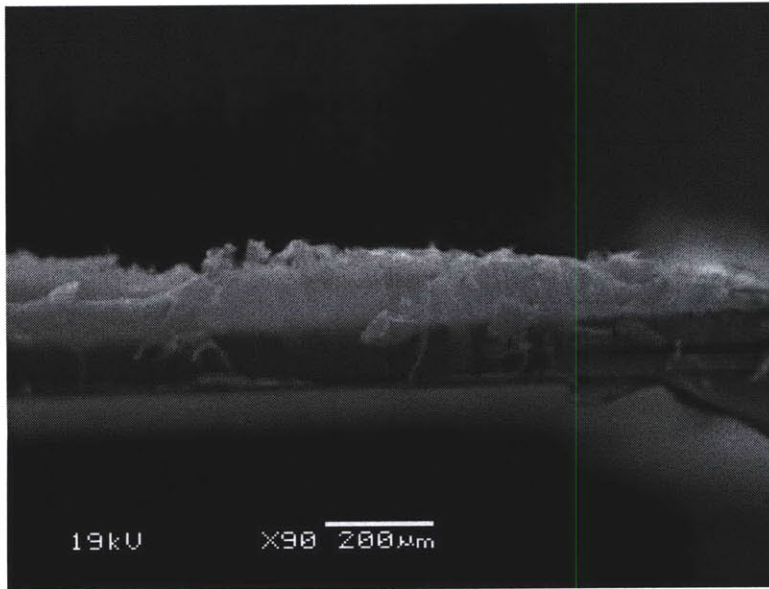
Figure 5.8: CNTs grown on a sputtered tungsten foil substrate. Uneven thickness is apparent throughout the sample.

The measured weight of the CNTs was only 0.3 mg. This low weight confirms the low density of the CNT array.

5.2 Comparison of Deposition Methods

Despite depositing equal thicknesses of both aluminum and iron, the difference in nanotube growth yield suggests that undesirable surface modifications are caused by the sputtering process.

E-beam deposition is considered very high purity because of the low background pressure, as previously discussed. Source atoms vaporized by the e-beam also contain very low amounts of energy (~0.1 eV). However, sputtering is high energy process. In addition to high energy target molecules contacting the surface (1-10 eV), inert or reactive gas ions may also deposit or impact the growing thin film. As a result, the surface topography of the sputtered samples is modified, causing more surface roughness and inhibiting nanotube growth.

AFM images comparing a tungsten foil substrate deposited with 15 nm of Al and 1.5 nm of Fe by e-beam and by sputtering are shown in Figure 5.9 and Figure 5.10, respectively. The topographic images show that catalyst layers deposited by sputtering result in larger nanoparticles than e-beam by a factor of two. Also, while the nanoparticles in the e-beam deposited sample are well-formed and distinct, the sputtered nanoparticles appear stretched. This may again be due to the high energy of the sputtering process, in which the collision of iron on the substrate causes the nanoparticles to flatten and grow in size.
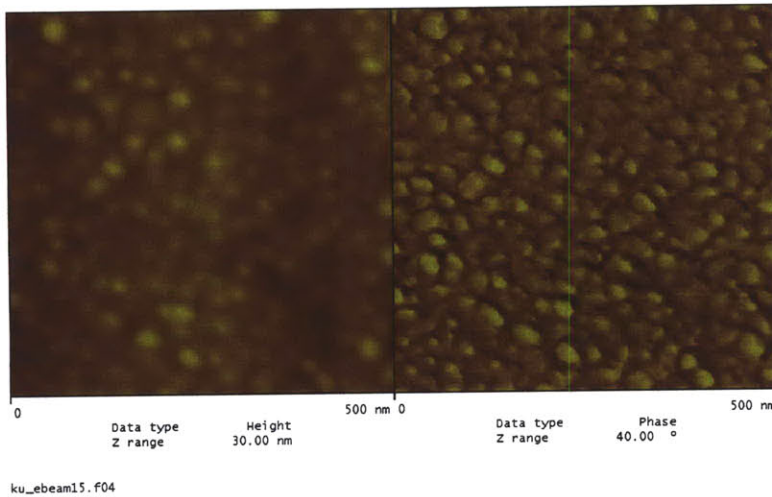
Figure 5.9: AFM image of tungsten foil deposited by electron beam evaporation with 15 nm of Al and 1.5 nm of Fe. Similar to Figure 3.12, nanoparticles are well formed and distinct, and are 25-30 nm in diameter.

ku_ebeam15.f04
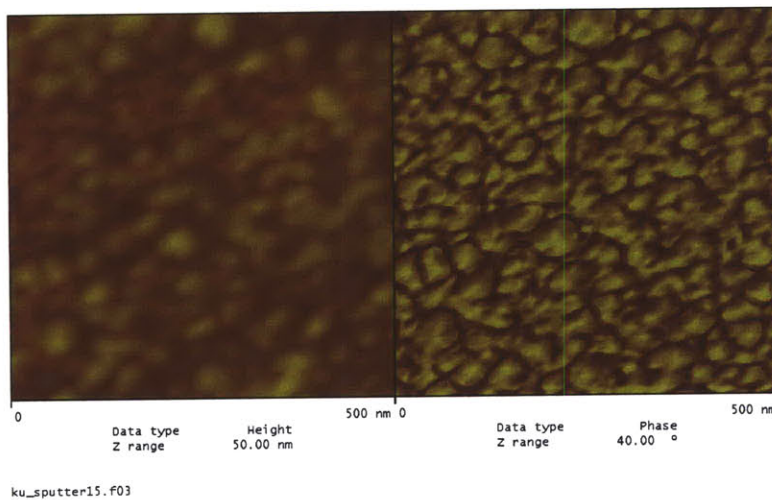
Figure 5.10: AFM image of tungsten foil deposited by sputtering with 15 nm of Al and 1.5 nm of Fe. In contrast to the e-beam deposition sample, nanoparticles are much larger (50-60 nm) and not as well-formed or distinct compared to e-beam deposition.

ku_sputter15.f03

A technique called resputtering may be evaluated as a possible method to smooth out the sputtered samples. Resputtering uses the plasma ions to dislodge the more loosely bound atoms in the film and re-deposit them in a nearby area to improve smoothness.

Future work can also explore other possible structural differences between e-beam and sputter deposited substrates. Ion bombardment during the sputter process may also cause crystallography changes, modifications of grain structure, and defects and stress in the deposited film.

6 Conclusion

6.1 Thesis summary

We have demonstrated the ability to grow a dense array of vertically aligned nanotubes on a variety of different conducting substrates using the CVD process. While a large portion of growth experiments was performed on tungsten substrates and tungsten foils, the successful growth of CNTs on aluminum foil represents a crucial step in realizing a commercial nanotube-enhanced ultracapacitor.

Although we have not reached the goal CNT density of 10^{12} CNTs/cm^2, we have made steady progress in increasing the CNT yield of our growth process. By decreasing surface roughness, decreasing the catalyst layer, and utilizing a quick heat up process, the density of the CNT array has increased from 10^{10} to 4×10^{11} CNTs/cm^2.

This thesis has not presented the data from device testing and modeling of electrochemical cells created using our fabricated nanotube electrodes. For further information, please reference Riccardo Signorelli's thesis [1].

We have met our goal of developing a CVD method to fabricate 1 cm^2 electrode samples on several different types of conducting substrates including inexpensive aluminum foils. Characterization of these electrodes demonstrates that we are close to our projected energy density projections. Table 6.1 below summarizes the targeted and achieved electrode specifications.

Table 6.1: Summary of targeted and achieved electrode specifications

	Targeted	Currently Achieved
Sample Size	1 cm^2	1 cm^2
CNT Length	150 μm	20-250 μm
CNT Diameter	4-7 nm	6.5 nm
CNT # of Walls	3	3-7
Growth on Al Foil	Yes	Yes
CNT Density	10^{12} cm^{-2}	$1\text{-}4 \times 10^{11}$ cm^{-2}

In order to reach these electrode specifications, a wide variety of different substrate materials, deposition techniques, and growth parameters were evaluated and optimized. After implementing each growth recipe, we adhered to a pattern of careful characterization, followed by improvements to the recipe based on theory and assessment of the results. This thesis has described the methodology in which these numerous different parameters were evaluated in order to achieve our goals.

6.2 Suggestions for Future Work

Further refinement in several areas of the growth process of CNTs is necessary in order to achieve a device suitable for commercialization. The need to improve the CNT density is critical. In addition, our model of a NEU has assumed idealized nanotubes that are free from defects and amorphous carbon. Surface modifications to the CNTs, such as oxidation, that are either able to remove amorphous carbon or purposefully produce advantageous defects may improve the performance of the device. For example, etching holes in the outer layers of CNT walls may increase the surface area and differential capacitance of the device.

Experimental growth has been limited to 1 cm^2 samples due to the size of the deposition chamber. A larger CVD system would allow for larger samples to be tested and would also allow for multiple samples to be tested in the same growth experiment.

Successful growth on sputter-deposited samples will be also be critical for any large scale growth. Although electron beam deposition is suitable for laboratory work, it is not suitable for manufacturing processes.

References

[1]   R. Signorelli, "High energy and power density nanotube-enhanced ultracapacitor design, modeling, testing, and predicted performance", Ph.D. thesis, Massachusetts Institute of Technology, 2009.

[2]   P.M. Parthangal, R.E. Cavicchi, M.R. Zachariah, "A generic process of growing aligned carbon nanotube arrays on metals and metal alloys", *Nanotechnology*, 18 (2007).

[3]   J. Schindall, "The charge of the ultra-capacitors", *IEEE Spectrum*, Nov. 2007, <http://www.spectrum.ieee.org/nov07/5636>.

[4]   R. Signorelli, J. Schindall, J. Kassakian, "Nanotube Enhanced Ultracapacitors", *International Seminar on Double Layer Capacitors and Hybrid Energy Storage Devices*, 14 (2004) 49-61.

[5]   A. C. Dupuis, "The catalyst in the CCVD of carbon nanotubes-a review", Progress in *Materials Science*, 50 (2005) 929–961.

[6]   C. Niu, E.K. Sichel, R. Hoch, D. Moy, and H. Tennent, "High power electrochemical capacitors based on carbon nanotube electrodes", *Applied Physics Letters*, 70(1996) 1480–1482.

[7]   S. Brunauer, P.H. Emmett, and E. Teller, "Adsorption of gases in multi-molecular layer", *J. Am. Chem. Soc*, 60 (1938) 309-319.

[8]   K.H. An, W.S. Kim, Y.S. Park, J. Moon, D.J. Bae, S.C. Lim, Y.S. Lee, and Y.H. Lee, "Electrochemical properties of high-power supercapacitors using single-walled carbon nanotube electrodes", *Advanced Functional Materials*, 11 (2001) 387–392.

[9]   B.J. Yoon, S.H. Jeong, K.H. Lee, H.S. Kim, C.G. Park, J.H. Han, "Electrical properties of electrical double layer capacitors with integrated carbon nanotube electrodes", *Chemical Physics Letters*, 388 (2004) 170–174.

[10]   C. Du and N. Pan, "Supercapacitors using carbon nanotubes films by electrophoretic deposition", *Journal of Power Sources*, 160 (2006) 1487–1494.

[11]   A. Kumar, V.L. Pushparaj, S. Kar, O. Nalamasu, and P.M. Ajayan, "Contact transfer of aligned carbon nanotube arrays onto conducting substrates", *Applied Physics Letters*, 89 (2006) 163120.

[12]   K. Hata, D. N. Futaba, K. Mizuno, T. Namai, M. Yumur, S. Iijima, "Water – Assisted Highly Effiecient Synthesis of Impurity-Free Single-Walled Carbon Nanotubes", *Science*, 306 (2004) 1362-1364.

[13]   D.N. Futaba, K. Hata, T. Yamada, T. Hiraoka, Y. Hayamizu, Y. Kakudate, O. Tanaike, H. Hatori, M. Yumura, and S. Iijima, "Shape-engineerable and highly densely packed single-walled carbon nanotubes and their application as super-capacitor electrodes", *Nature*, 5 (2006) 987-994.

[14]   I.K. Song, Y.S. Cho, G.S. Choi, J.B. Park, and D.J. Kim, "The growth mode change in carbon nanotube synthesis in plasma-enhanced chemical vapor deposition", *Diamond and Related Materials*, 13 (2004) 1210–1213.

[15]   H. Dai, "Carbon Nanotubes: Synthesis, Integration, and Properties", *Acc. Chem. Res.*, 35 (2002) 1035-1044

[16]   A. Cassell, J.A. Raymakers, J. Kong, and H. Dai, "Large Scale CVD Synthesis of Single-Walled Carbon Nanotubes", *J. Phys. Chem. B.*, 103 (1999) 6484-6492.

[17]   A.A. Puretzky, D.B. Geohegan, S. Jesse, I.N. Ivanov, and G. Eres, "In situ measurements and modeling of carbon nanotube array growth kinetics during chemical vapor deposition", *App. Phys. A*, 81 (2005) 223-240.

[18]   G. Eres, A. A. Kinkhabwala, H. Cui, D.B. Geohegan, A.A. Puretzky, and D. Lowndes, "Molecular Beam-Controlled Nucleation and Growth of Vertically Aligned Single-Wall Carbon Nanotube Arrays", *J. Phys. Chem. B*, 109 (2005) 16684-16694.

[19]   C. Emmenegger, J.M. Bonard, P. Mauron, P. Suda, A. Lepora, B. Groberty, A. Zuttel, L. Schlapbach, "Synthesis of carbon nanotubes over Fe catalyst on aluminum and suggested growth mechanism", *Carbon*, 41 (2003) 539-547.

[20]   S.B. Sinnott, R. Andrews, D. Quian, A.M. Rao, Z. Mao, E.E. Dickey, F. Derbyshire. "Model of carbon nanotube growth through chemical vapor deposition". *Chem. Phys. Letters*, 315 (1999) 25-30.

[21]   S. Naha, I. Puri, "A model for catalytic growth of carbon nanotubes", *J. Phys. D: Appl. Phys.*, 41 (2008) 1-6.

[22]   H. Liu, D. Dandy, "Nucleation kinetics of diamond on carbide-forming substrates during chemical vapor deposition", *J. Electrochem. Soc.*, 143 (1996) 1104-1109.

[23] R. Sharma, P. Rez, M. Brown, G. Du, M.M. Treacy, "Dynamic observations of the effect of pressure and temperature conditions on the selective synthesis of carbon nanotubes", *Nanotechnology*, 18 (2007) 1-8.

[24] R.H. Baughman, A.A. Zakhidov, W.H. de Heer, "Carbon Nanotubes-the route toward applications", *Science*, 292 (2002) 787-792.

[25] L.V. Laake, A.J. Hart, A.H. Slocum, "Suspended heater silicon platform for rapid thermal control of surface reactions with application to carbon nanotube synthesis", *Rev. of Sci. Instr.*, 18 (2007).

[26] C. Zhang, S. Pisana, C.T. Wirth, A. Parvec, C. Ducati, S. Hofmann, J. Robertson, "Growth of aligned millimeter-long carbon nanotube by chemical vapor deposition", *Diamond & Rel. Mat.*, 17 (2008) 1447-1451.

[27] K. Hata, D. Futaba, K. Mizuno, T. Namai, M. Yumura, S. Iijima, "Water-assisted highly efficient synthesis of impurity-free single-walled carbon nanotubes", *Science*, 306 (2004) 1362-1364.

[28] S. Hofmann, R. Blume, C.T. Wirth, M. Cantoro, R. Sharma, C. Ducati, et al, "State of Transition metal catalysts during carbon nanotube growth", *J. of Phys. Chem. C.*, 113 (2009) 1648-1656.

[29] S.B. Sinnott, R. Andrews, D. Quian, A.M. Rao, Z. Mao, E.C. Dickey, F. Derbyshire, "Model of carbon nanotube growth through chemical vapor deposition", *Chemial Physics Letters*, 315 (1999) 25-30.

[30] C. Klinke, J.M. Bonard, K. Kern, "Comparative study of the catalytic growth of patterned carbon nanotube films", *Surf Sci*, 492 (2001), 195–201

[31] K. Hernadi, A. Fonseca, J.B. Nagy, A. Siska, I. Kiricsi, "Production of nanotubes by the catalytic decomposition of different carbon-containing compounds", *Appl Catal A*, 199 (2000) 245–255

[32] J. Kong, A.M. Cassel, H. Dai, "Chemical vapor deposition of methane for single-walled carbon nanotubes", *Chem Phys Lett.* 292 (1998) 567–574.

[33] L. Delzeit, B. Chen, A. Cassell, R. Stevens, C. Nguyen, M. Meyyappan, "Multilayered metal catalysts for controlling the density of single-walled carbon nanotube growth", *Chem. Phys. Lett.*, 348 (2001) 368–74.

[34] A.J. Hart, A.H. Slocum, L. Royer, "Growth of conformal single walled carbon nanotube films from Mo/Fe/Al$_2$O$_3$ deposited by electron beam evaporation", *Carbon*, 44 (2006) 348-359.

[35] W.Q. Deng,, X. Xu, W.A. Goddard, "A two-stage mechanism of bimetallic catalyzed growth of single-walled carbon nanotubes", *Nano Letters*, 4 (2004) 2331–2335.

[36] F.O. Jones, K.O. Wood, "The melting point of thin aluminum films", *Brit. J. Appl. Phys* 15 (1965) 185-187.

[37] T. de los Arcos, Z.M. Wu, P. Oelhafen, "Is aluminum a suitable buffer layer for carbon nanotube growth?", *Chem. Phys. Letters* 380 (2003) 419-423.

[38] M.A. Ermakova, D.Y. Ermakov, A.L. Chuvilin, G.G. Kuvshinov, "Decomposition of methane over iron catalysts at the range of moderate temperatures: the influence of structure of the catalytic systems and the reaction conditions on the yield of carbon and morphology of carbon filaments", *J. Catal.*, 201 (2001) 183-197.

[39] S.S. Pan, Z.W. Xie, B.H. Chang, L.F. Sun, W.Y. Zhou, G. Wang, "Direct growth of aligned open carbon nanotubes by chemical vapor deposition", *Chem. Phys. Letters*, 299 (1999) 97-102.

[40] P. Chen, H.B. Zhang, G.D. Lin, Q. Hong, K.R. Tsai, "Growth of carbon nanotubes by catalytic decomposition of CH_4 or CO on Ni-MGO catalyst", *Carbon*, 35 (1997) 1495.

[41] K. Hernadi, A. Fonseca, J.B. Nagy, D. Bernaerts, A. Fudala, A.A. Lucas, "Catalytic synthesis of carbon nanotubes using zeolite support", *Zeolites*, 17 (1996) 416-423.

[42] A. Fonseca, K. Hernadi, J.B. Nagy, D. Bernaerts, A.A. Lucas, "Optimization of catalytic production and purification of buckytubes", *J. Mol. Catal. A*, 107 (1996) 159-168.

[43] Y.J. Yoon, J.C. Bae, H.K. baik, S.J. Cho, S.J. Lee, K.M. Song, "Growth control of single and multi-walled carbon nanotubes by thin film catalyst", *Chem Phys. Letters*, 366 (2002) 109-114.

[44] Z.F. Ren, Z.P. Huang, J.W. Xu, J.H. Wang, P. Bush, M.P. Sigal, "Synthesis of large arrays of well-aligned carbon nanotubes on glass", *Science*, 282 (1998) 1105-1107.